Front. Phys. 13(6), 132108 (2018)
https://doi.org/10.1007/s11467-018-0830-y

REVIEW ARTICLE

Coexistence of cluster and shell-model aspects in nuclear systems

Yoshiko Kanada-En'yo[1,†], **Hisashi Horiuchi**[2]

[1] *Department of Physics, Kyoto University, Kitashirakawa Oiwake-Cho, Kyoto 606-8502, Japan*
[2] *Research Center for Nuclear Physics (RCNP), Osaka University, Ibaraki, Osaka 567-0047, Japan*
Corresponding author. E-mail: [†] *yenyo@ruby.scphys.kyoto-u.ac.jp*
Received June 11, 2018; Accepted July 4, 2018

We discuss cluster phenomena in light nuclei. As examples of typical cluster structures, we first review cluster structures of ^{12}C, ^{16}O, and ^{20}Ne, and then introduce some topics of cluster phenomena in light neutron-rich nuclei such as Be and C isotopes. A particular attention is paid on coexistence of cluster and shell-model aspects.

Keywords cluster, nuclear structure

PACS numbers 02.70.Ns, 21.60.-n, 21.10.Ft

Contents

1 Cluster and shell-model aspects

A nucleus is a finite quantum many-body system consisting of protons and neutrons. It is a self-bound system, in which nucleons are attracted between each other by nuclear forces and bound without external potentials. It is a clear difference from an electron system, where electrons are bound in the external Coulomb potential from a nucleus located at the center. Nevertheless, the mean-field picture works at the leading order at least in low-lying states, namely, nucleons behave as independent particles in the mean-field resulting in shell structures. However, correlations between nucleons are, of course, rather strong because of the attractive nuclear forces. A typical example of the multi-nucleon correlations is "cluster", which is a subunit formed by spatially correlated nucleons. In other words, two different natures, the independent-particle (mean-field) feature and the cluster feature coexist in nuclear systems. As a result of the coexistence, rich phenomena appear depending on proton and neutron numbers, energy, and density of the system.

If there is no correlation between nucleons, all nucleons behave as independent particles in the mean-field and form a clear Fermi surface, i.e., the shell structure. However, in reality, correlations between nucleons are rather

*Special Topic: Simplicity, Symmetry, and Beauty of Atomic Nuclei (Eds. Jie Meng, Takaharu Otsuka & Yu-Min Zhao).

Frontiers of Physics

strong due to the attractive nuclear forces. As a result of the multi-nucleon correlations, clusters often emerge at the nuclear surface as a kind of the ground state correlation because of the residual interactions from the attractive nuclear forces. This is nothing but the cluster formation, which is often found, in particular, in low-lying states of light nuclei. At this stage of the cluster formation in low-lying states, clusters are still largely overlapping with each other and the system is a compact state with the normal density. Once clusters are formed in the system, inter-cluster motion can be easily activated with only small amount of energy. Then, spatially developed cluster structures appear in excited states because of excitation of the inter-cluster motion, and the system goes to a low-density state. It means that, there are two stages of clustering in nuclei; one is the cluster formation phase and the other is the cluster excitation phase. The former, cluster formation, is caused by many-nucleon correlations at the nuclear surface and smoothly connected to the independent-particle (mean-field) feature through the cluster melting or breaking. However, the latter, cluster excitation, is a unique feature beyond the mean-field picture, which is characterized by large amplitude mode of the inter-cluster motion decoupled from single-particle modes.

^{12}C is a typical example of the cluster and mean-field coexisting systems. The ground state of ^{12}C is the mean-field (shell-model-like) state dominated by the $p_{3/2}$-subshell closed configuration with significant mixing of the 3α-cluster component. It means that α clusters are partially formed even in the ground state of ^{12}C. At approximately 100 MeV excitation energy, all twelve nucleons in ^{12}C can dissociate, and the system goes to a free nucleon gas state in a low density limit. At approximately 10 MeV, much lower energy than the free nucleon gas, three α clusters develop spatially in excited states of ^{12}C. This energy for 3α-cluster excitation is much smaller than that of the free nucleon gas state, meaning that the mean-field and cluster states coexist in low-energy levels of ^{12}C. As the excitation energy increases from the ground to cluster excited states, density of the system changes from normal density to low density, meaning that, in a sense, one can control the density of the system by changing the excitation energy. Generally, cluster features are enhanced at a relatively low density region, typically $(1/3)\rho_0 \sim (1/5)\rho_0$ as can be seen from remarkable cluster structures at nuclear surface, in light-mass nuclei as well as excited states.

α cluster is known to be one of the most important and fundamental cluster units. ^{4}He is the most smallest shell closed state with saturated spin and isospin, and a robust object against the internal excitation as known from the extremely high excitation energy $E_x \sim 20$ MeV for the first excited state. Therefore, the α cluster can be a building block of cluster structures in heavier systems such as $n\alpha$ cluster structures in $Z = N =$ even nuclei. For instance, the ground state of ^{8}Be is understood as a quasi-bound 2α state, in which two α clusters are rather weakly interacting. Also in $A \gtrsim 12$, developed 3α- and ^{12}C+α-cluster structures in ^{12}C* and ^{16}O* have been considered to describe energy spectra.

In the mean-field picture, the formation of α clusters is not obvious. In 1950s–1970s, the cluster formation has been discussed from the point of view of multi-nucleon correlations in the shell model to understand structures of p-shell and sd-shell nuclei. In particular, a central issue is to describe α cluster states with four-nucleon correlation in a shell. In discussing the formation of clusters in the shell-model picture, the duality character of the harmonic oscillator shell model wave function was recognized already in 1950s among people who studied microscopic cluster model. For example, Perring and Skyrme discussed in their paper [1], that it is possible to write down alpha-particle wave functions for the ground states of ^{8}Be, ^{12}C, and ^{16}O, which become identical with shell-model wave functions when they are antisymmetrized. According to the Bayman-Bohr theorem [2] which describes the duality character of the shell model wave function, the ^{20}Ne ground state having the spatial symmetry [4] and the SU(3) symmetry $(\lambda, \mu) = (8, 0)$ for the valence 2 neutrons and 2 protons in sd-shell outside of the ^{16}O core has the clustering structure of ^{16}O+α. This shows the spatial and SU(3) symmetry of the four-nucleon correlation has the alpha-clustering nature. In relation to this, the core-excited states of ^{16}O $\sim$ ^{19}F (^{19}Ne) with the configurations having four nucleons in sd-shell were discussed to be related to the cluster states of ^{12}C+α $\sim$ ^{15}N+α (^{15}O+α) [3, 4].

Since 1960s, theoretical researches with microscopic cluster models have been made progress to investigate details of cluster phenomena mainly in stable nuclei. In the early stage, scattering between very light nuclei has been studied with the resonating group method (RGM) [5–8]. Since 1970's, thanks to application of the generator coordinate method (GCM) [9, 10] with the Bloch–Brink cluster wave function [11], microscopic studies of cluster phenomena has been extended to heavier systems such as p-shell and sd-shell nuclei.

In these decades, further advances of the cluster physics have been made owing to experimental and theoretical progresses in physics of unstable nuclei. A variety of cluster structures have been discovered also in neutron-rich nuclei. Microscopic cluster models have been extended to deal with the cluster structures with excess neutrons. Moreover, more flexible methods such as antisymmetrized molecular dynamics (AMD) [12–17] and fermionic molecular dynamces (FMD) [18–22] have been developed since 1990s.

The AMD and FMD wave functions are based not on cluster degrees of freedom but on nucleon degrees of freedom. In this sense, these models are not cluster models. Nevertheless, the AMD (FMD) model contains various cluster states in its model space, and therefore, it enables us to investigate cluster phenomena in general nuclei including exotic nuclei. Another advantage is that the model contains also mean-field states and can describe the coexistence of mean-field and cluster aspects without relying on *a priori* assumption of clusters. It is a great merit of the AMD to investigate cluster formation and breaking in the ground and excited states. In systematic studies of *p*-shell and *sd*-shell nuclei with the AMD, it has been revealed that the interplay between cluster and mean-field features plays an key role in both low-energy states and excitation modes. The cluster formation in the mean-field picture (or cluster breaking in the cluster picture) occurs in low-lying states as one can see the cluster correlation even in the ground states as the ground state correlations. In excitation modes, large amplitude inter-cluster dynamics gives significant contribution to low-energy monopole and dipole modes, whereas coherent 1p-1h excitations describe the high-energy giant resonance modes. In order to figure out the fundamental physics behind rich exotic phenomena discovered in unstable nuclei, it is essential to clarify the two stages of clustering, the cluster formation and the large amplitude inter-cluster motion.

In this paper, we discuss cluster phenomena in ^{12}C, ^{16}O, and ^{20}N focusing on the interplay between cluster and shell-model aspects. Some topics of light unstable nuclei are also discussed. Major parts of the discussions in the present paper are based on theoretical works done with the AMD method. For the details of the AMD frameworks, the reader is referred to recent review articles [17, 23] and references therein.

This article is organized as follows. In the next section, we briefly review the microscopic cluster models and the AMD model. Sections 3, 4, and 5 discuss cluster structures in ^{12}C, ^{16}O, and ^{20}Ne, respectively. Section 6 covers some topics of cluster structures in neutron-rich nuclei. Finally, a summary is given in Section 7.

2 Microscopic frameworks for cluster structures

2.1 Cluster models

Microscopic cluster models have been developed and applied to investigate various cluster phenomena. Microscopic studies started from the RGM [5–8], which has been intensively applied for scattering between light nuclei in 1960s and 1970s. Since 1970s, microscopic studies of cluster phenomena in heavy mass and many-cluster systems [24] have been performed with the GCM [9, 10] using the Bloch–Brink cluster wave function [11].

In the RGM for a single-channel case of two clusters C_1 and C_2, the model wave function is expressed as

$$\Psi_{\rm RGM} = \mathcal{A}\left\{\phi(C_1)\phi(C_2)\chi(\boldsymbol{\xi})\right\}, \tag{1}$$

where $\mathcal{A}$ is the nucleon antisymmetrizer, $\phi(C_i)$ is the internal wave function of the C_i-cluster, and $\boldsymbol{\xi}$ is the relative coordinate between the centers of mass of the clusters. The inter-cluster wave function $\chi(\boldsymbol{\xi})$ is determined by solving the RGM equation. In the RGM for coupled-channel problems, distortion of clusters and multi-channel systems can be taken into account.

In the GCM approach, the Bloch–Brink cluster wave function is adopted as a basis wave function [11],

$$\Phi_{\rm BB}(\boldsymbol{S}_1,\cdots,\boldsymbol{S}_k) = n_0\mathcal{A}\left\{\psi(C_1;\boldsymbol{S}_1)\cdots\psi(C_k;\boldsymbol{S}_k)\right\}, \tag{2}$$

where the ith cluster (C_i) is localized around $\boldsymbol{S}_i$. The wave function $\psi(C_i;\boldsymbol{S}_i)$ for the ith cluster is written in terms of the harmonic oscillator shell-model wave function placed at $\boldsymbol{S}_i$. In the case that cluster is located far from each other, the parameter $\boldsymbol{S}_i$ indicates the mean center position of the cluster. In the short distance (small $|\boldsymbol{S}_i|$) case that clusters largely overlap with each other, the Bloch–Brink cluster wave function becomes the specific shell-model configuration (the SU(3) shell model wave function) because of antisymmetrization of nucleons between clusters. Thus, a spatially developed cluster state can be smoothly connected to the shell-model limit by the position parameters $\{\boldsymbol{S}_1,\cdots,\boldsymbol{S}_k\}$.

For detailed description of the inter-cluster motion, the Bloch–Brink wave functions are superposed in the GCM by treating the cluster center parameters $\{\boldsymbol{S}_1,\cdots,\boldsymbol{S}_k\}$ as generator coordinates,

$$\Psi_{\rm GCM} = \int {\rm d}\boldsymbol{S}_1,\cdots,{\rm d}\boldsymbol{S}_k f(\boldsymbol{S}_1,\cdots,\boldsymbol{S}_k) \times P^{J\pi}_{MK}\Phi_{\rm BB}(\boldsymbol{S}_1,\cdots,\boldsymbol{S}_k), \tag{3}$$

where $P^{J\pi}_{MK}$ is the total-angular momentum and parity projection operator, and coefficients $f(\boldsymbol{S}_1,\cdots,\boldsymbol{S}_k)$ are determined by solving the Hill–Wheeler equation [9], in practical, diagonalization of Hamiltonian and norm matrices.

2.2 Antisymmetrized molecular dynamics

The AMD method is an approach which treats nucleon degrees of freedom independently without assuming any clusters. Nevertheless, the AMD can describe various cluster structures because the Bloch–Brink cluster wave functions for any cluster channels are included in the AMD model space.

An AMD wave function is given by a Slater determinant of single-nucleon Gaussian wave functions,

$$\Phi_{\rm AMD}(\boldsymbol{Z}) = \frac{1}{\sqrt{A!}}\mathcal{A}\{\varphi_1, \varphi_2, \cdots, \varphi_A\}, \tag{4}$$

where the ith single-particle wave function φ_i is written by a product of spatial, spin, and isospin wave functions as

$$\varphi_i = \phi_{\boldsymbol{X}_i}\chi_i\tau_i, \tag{5}$$

$$\phi_{\boldsymbol{X}_i}(\boldsymbol{r}) = \left(\frac{2\nu}{\pi}\right)^{4/3} \exp\{-\nu(\boldsymbol{r}-\boldsymbol{X}_i)^2\}, \tag{6}$$

$$\chi_i = \left(\frac{1}{2}+\xi_i\right)\chi_\uparrow + \left(\frac{1}{2}-\xi_i\right)\chi_\downarrow. \tag{7}$$

$\phi_{\boldsymbol{X}_i}$ and χ_i are the spatial and spin functions, respectively, and τ_i is the isospin function fixed to be proton or neutron. The width parameter ν is taken to be a common value for all nucleons and optimized for each nucleus.

In the AMD wave function, the ith single-particle wave function is expressed by the Gaussian wave packet localized around the position $\boldsymbol{X}_i$. The Gaussian center positions $\{\boldsymbol{X}_i\}$ and the intrinsic-spin orientations $\{\xi_i\}$ for all nucleons are independently treated as variational parameters which are determined by energy variation.

In the AMD wave function, the Brink–Bloch cluster wave functions can be described by the corresponding configuration of Gaussian center positions. Or, if Gaussian centers are located at short distances between each other, the AMD wave function is equivalent to a harmonic oscillator shell-model wave function. Moreover, it can continuously connect remarkable cluster and mean-field structures through cluster dissolution/formation. This is a great advantage superior to cluster models and mean-field approaches. Because of this flexibility of the model wave function, the AMD is an useful approach for cluster and mean-field aspects in the ground and excited states and applicable to general nuclei.

It should be commented that, a similar wave function is used in the fermionic molecular dynamics (FMD) developed by Feldmeier and Neff, and their collaborators [18–21].

In the AMD framework for structure study, energy variation (energy optimization) after the parity projection is performed within the AMD model space to obtain the ground state wave function. With regard to the angular-momentum projection, the variational method before the projection (VBP) is usually applied in the simple AMD [15], whereas the variation after the projection (VAP) is performed in the AMD+VAP method [25]. For the description of excited states, the AMD wave functions obtained by the energy variation are superposed. To efficiently choose basis AMD wave functions for the superposition, constraint versions of the AMD are often combined with the GCM (AMD+GCM). In the β-constraint ($\beta\gamma$-constraint) AMD [26, 27], the energy variation is done under constraints on deformation parameters β (and γ), respectively. After the energy variation with the constraints, the obtained AMD wave functions are superposed with the GCM treatment. The framework AMD+GCM can microscopically treat large amplitude dynamics along the generator coordinates.

Although the AMD+GCM is useful for large amplitude collective motion, it is not sufficient for single-particle excitations on top of a mean-field state because basis wave functions for the superposition are usually prepared by the energy variation and only the modes along adopted generated coordinates can be described. To overcome this problem, the shifted basis AMD (sAMD) [28–30] has been proposed, which is useful to describe small amplitude modes on the ground state. In the sAMD, small shift of Gaussian center position of each single-particle wave function from the ground state AMD wave function is considered, and all the shifted basis wave functions are superposed to describe linear combinations of one-particle and one-hole (1p-1h) excitations. The method combined with the cluster GCM has been applied to monopole and dipole excitations in light nuclei and proved to be able to describe coexistence of low-energy cluster modes and high-energy giant resonances.

3 Clustering in ^{12}C

3.1 Overview of cluster aspects in ^{12}C

^{12}C is a fascinating nuclei, which has been intensively studied in experimental and theoretical researches for a long time. As mentioned previously, its ground state shows both the $p_{3/2}$-closure feature (shell-model aspect) and 3α correlation (cluster aspect). In its excited states, various 3α cluster structures emerge from the large amplitude inter-cluster motion as they have been discovered in theoretical and experimental works (for example, Refs. [24, 31] and references therein). Indeed, remarkable 3α cluster states, for instance, ^{12}C(0^+_2) and ^{12}C(3^-_1), have been obtained with (semi) microscopic and non-microscopic 3α-cluster models [32–44]. The former is a weakly bound 3α state, in which α clusters are moving freely like a gas. The latter is understood as the band-head state of the $K^\pi = 3^-$ band constructed by a regular triangle 3α configuration of the intrinsic state.

In spite of success of 3α-cluster models in describing many excited states of ^{12}C, the cluster models are not sufficient to quantitatively reproduce properties of low-lying states such as large level spacing between the 0^+_1 and 2^+_1 states and significant β transitions from ^{12}B, because the α-cluster breaking is not taken into account

in the models. Moreover, since clusters are *a priori* assumed in the models, it is not able to check the α cluster formation in 12-body dynamics.

These problems have been overcome by the AMD and FMD models. In AMD and FMD studies of ^{12}C, it has been shown that [22, 25, 45, 46], 3α-cluster structures are actually formed without assuming existence of α clusters. To describe details of 3α dynamics in excited states, hybrid models of the AMD and FMD models combined with the 3α GCM have been also applied. Recently, study of cluster structures of ^{12}C with *ab initio* calculations are being developing [47–49].

3.2 Hybridization of shell model and 3α cluster model

The coexistence and coupling of shell-model and cluster structures in ^{12}C were first studied in detail by Takigawa and Arima [50] by adopting the hybridization of wave functions of shell model and 3α cluster model. For describing α clustering, they used 3α Bloch–Brink wave functions with regular triangle and linear chain configurations of α clusters with parity and angular momentum projection. These cluster wave functions are linearly combined with intermediate-coupling 0p-shell model wave functions like $|p^8[431]^{13}P_0\rangle$. The ground-band states have non-zero inter-cluster distance although they are much smaller than those in other excited states like 3^-_1 and 0^+_2. It was found that in the ground band the coupling to 0p-shell model wave functions with broken spatial symmetry which is caused by the spin-orbit interaction is very important for raising the excitation energies of 2^+_1 and 4^+_1 states which are too small with only 3α cluster wave functions with good spatial symmetry [444].

The $B(E2)$ transition value $B(E2, 0^+_2 \rightarrow 2^+_1)$ and monopole transition value $M(0^+_2 \rightarrow 0^+_1)$ are the transition strengths between clustering excited states and the ground band states. These values were reproduced well in Ref. [50]. As for the inelastic electron scattering form factor for $0^+_1 \rightarrow 0^+_2$, the reproduction of the data is good for low transfer momentum q because the $M(0^+_2 \rightarrow 0^+_1)$ is reproduced well, but for high q beyond the peak of the form factor the calculation underestimates the data. On the other hand, microscopic cluster models which adopt 3α RGM wave function [33] and 3α THSR (Tohsaki–Horiuchi–Schuck–Roepke) wave function [51] reproduce the inelastic form factor well up to high transfer momentum q although the reproduction in the very low momentum region is slightly overestimated as seen in slightly overestimated $M(0^+_2 \rightarrow 0^+_1)$. Since these cluster model wave functions have totally symmetric spatial symmetry [444] even for the ground state, we wonder how the improved wave functions containing non-[444] symmetry components obtained by including the effects of spin-orbit and tensor forces can give again the good reproduction of the form factor. In this respect it is very instructive that the recent *ab initio* calculation of the ground and the Hoyle state (0^+_2) by the quantum Monte Carlo method gives fairly good reproduction of the inelastic form factor [49].

3.3 Cluster structures in ^{12}C studied with AMD

The AMD with the variation after spin-parity projections (AMD+VAP) was applied to ^{12}C [25, 45]. The calculated energy levels of ^{12}C are shown in Fig. 1. The intrinsic density distribution of the dominant component for each state is also shown. The calculation reproduces well the experimental spectra of the $K^\pi = 0^+_1$, $K^\pi = 0^+_2$, and $J^\pi = 1^+$ states as well as negative-parity bands $K^\pi = 3^-_1$, and $K^\pi = 1^-_1$. The intrinsic state of the $K^\pi = 0^+_1$ band shows a compact 3α cluster structure. The band head, ^{12}C(0^+_1), contains the significant cluster breaking component, which is necessary to obtain extra energy gain of the spin-orbit force. In other words, the cluster breaking is essential to reproduce the large 0^+-2^+ level spacing. ^{12}C(0^+_2) is described by superposition of various 3α configurations showing the cluster gas nature that 3α clusters are weakly interacting in a dilute density like a gas. This is consistent with other microscopic 3α cluster model calculations. The experimental 2^+_2 and 4^+_1 states observed recently are assigned to the $K^\pi = 0^+_2$ band starting from ^{12}C(0^+_2). However, the strong $E2$ transitions from 2^+_2 to the 0^+_2 and 0^+_3 states obtained in the AMD+VAP calculation indicate signifi-

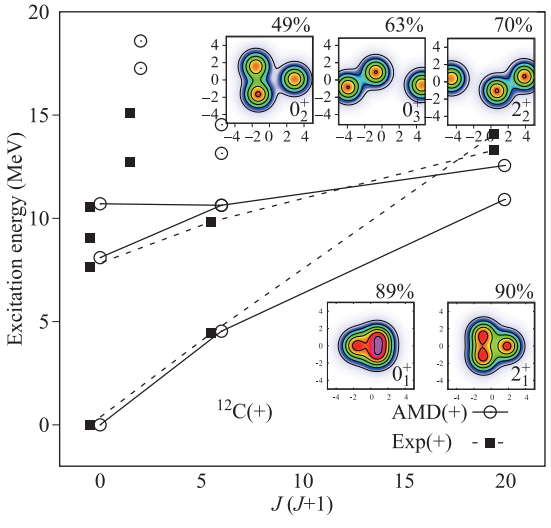

Fig. 1 Positive-parity energy levels of ^{12}C. The energies obtained by the AMD+VAP using the MV1 force [45] together with the experimental positive-parity energy spectra [52–56]. Matter density distribution of dominant intrinsic wave functions is shown with percentages in the final wave function. Reproduced from Ref. [57].

cant state mixing (or structure change) between the two 0^+ states (0^+_2 and 0^+_3). It suggests that the 0^+_2 state may be a fragile object against rotation of the system.

It it instructive to consider the shell model basis expansion of cluster states. An α cluster is the strongly correlated object composed of four nucleons. If one finds a nucleon in the α cluster at a certain position, one should find other three nucleons in its vicinity. In the harmonic oscillator basis expansion for such the highly correlated subsystem, a huge number of basis wave functions with high angular momenta are contained in the wave function as easily understood by the Heisenberg uncertainty principle. In other words, spatially developed cluster states are highly correlated states beyond mean-field approximations, and therefore, such the states are usually missing in calculated low-energy spectra obtained by traditional shell-model calculations.

To demonstrate how the cluster states in ^{12}C contain high-shell components, we show the occupation probability of harmonic oscillator quanta N in the shell-model basis expansion in Fig. 2. Here, the size parameter of the harmonic oscillator is fixed to be $b = 1/\sqrt{2\nu}$. The 0^+_1 is dominantly described by the $0\hbar\omega$ configuration but it contains 20% mixing of higher shell configurations corresponding to the ground state correlation due to mixing of the cluster component. It indicates that higher shell components are significantly contained even in the ground state. In contrast to the dominant $0\hbar\omega$ configuration in the ground state, the occupation probability of the 0^+_2 is distributed broadly in the high shell region because of the spatial developed 3α-cluster structure. In particular, tiny percents are fragmented in the extremely high N region, which are far from the mean-field model space. Similarly to the 0^+_2 state, the 1^-_1 state also shows very broad distribution of the occupation probability because of the developed cluster structure with a open triangle configuration. More details of structures of 1^- states are discussed later.

3.4 Cluster breaking effect in ^{12}C

3α-cluster breaking component plays an important role to reproduce the large 0^+_1-2^+_1 level spacing. Moreover, the cluster-breaking component contained in the 0^+_1 affects the 3α cluster structures in excited 0^+ states through the orthogonality to the ground state and somewhat changes energy spectra and band structures of 3α-cluster states.

The cluster breaking component in the ^{12}C(0^+_1) is mainly contributed by the $p_{3/2}$-shell closed configuration. Both the SU(3)-limit 3α and $p_{3/2}$ configurations are included in the $0\hbar\omega$ configurations of the ^{12}C system. On the other hand, the spatial development of the 3α cluster structure involved mixing of high-shell components. In order to smoothly connect the spatially developed 3α, SU(3)-limit 3α, and $p_{3/2}$ states, the antisymmetrized quasi cluster model (AQCM) has been proposed [59, 62]. In this model, the ^{12}C wave function is parametrized by the distance D between α clusters and the cluster breaking parameter Λ. We show, in Fig. 3, the 0^+ energy surface on the Λ-D plane calculated with the AQCM wave function. On the Λ-D plane, the SU(3)-limit 3α configuration can be smoothly connected to the $p_{3/2}$ configuration by controlling the cluster breaking parameter Λ on the $D \sim 0$ line, whereas it is connected to the spatially developed 3α state by changing the distance parameter

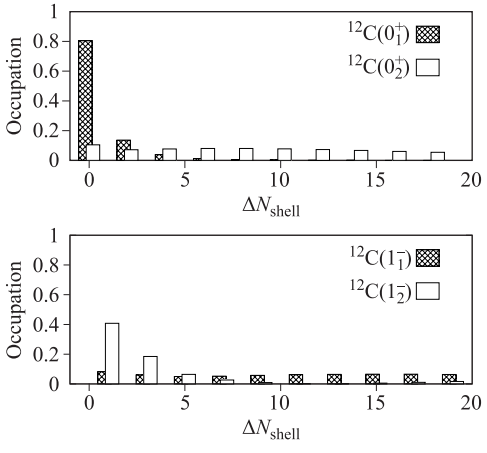

Fig. 2 Occupation probability of harmonic oscillator quanta N in the shell-model basis expansion of the $0^+_{1,2}$ and $1^-_{1,2}$ states obtained by the sAMD+3αGCM. The horizontal axis indicates the difference ΔN from the minimum quanta $N_{\rm min} = 8$. Reproduced from Ref. [58].

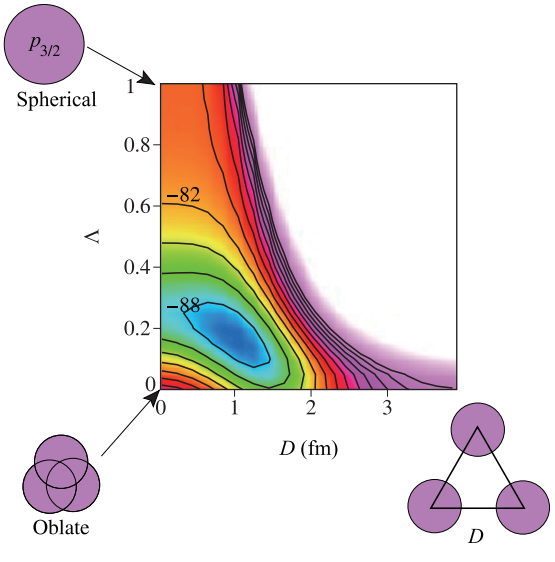

Fig. 3 0^+-projected energy of ^{12}C calculated by the AQCM. The energy surface on the Λ-D plane is shown. The interaction and width parameters are same as those in Ref. [59]. Reproduced from Ref. [57].

D. The energy surface shows the energy minimum for ^{12}C(0^+_1) at finite D and Λ values, which correspond to the ground state correlation beyond $0\hbar\omega$ configuration ($D \neq 0$) and significant mixing of the cluster breaking ($\Lambda \neq 0$).

The cluster breaking component in the ^{12}C(0^+_1) does not give drastic effects to excited 3α cluster states. However, it affects more or less the structures of excited 0^+ states through the orthogonality to the ground state. Therefore, one can see quantitative differences between model calculations with and without inclusion of the cluster breaking. For example, the AMD and FMD calculations show trend of a larger 0^+_2-2^+_2 level spacing than that obtained by 3α calculations without the cluster breaking, because the cluster breaking in the ^{12}C(0^+_1) causes energy shift of excited 0^+ states.

Suhara and Y. K-E. investigated the cluster breaking effects on 3α cluster structures in ^{12}C by explicitly adding the $p_{3/2}$ closed-shell configuration (cluster breaking component) into the 3α GCM calculation [60]. Figure 4 shows the comparison of the calculated energy spectra with and without the $p_{3/2}$ configuration. In the calculation with the $p_{3/2}$ configuration, ^{12}C(0^+_1) gains the extra energy of the spin-orbit attraction. It should be pointed out that inclusion of the $p_{3/2}$ configuration also lowers the energy of the 0^+_2 and 0^+_3 states. As a result of the global energy shift of the ground and excited 0^+ states, the 2^+_1 and 2^+_2 energies are raised up relatively to the 0^+_1, 0^+_2, and 0^+_3 ones.

The cluster breaking also affects to the $E2$ transitions. $B(E2)$ values calculated by microscopic models are summarized in Table 1. For the $E2$ transition from the 2^+_2, the 3α cluster models give the largest $B(E2)$ of $2^+_2 \to 0^+_2$ and relatively weaker $E2$ transition of $2^+_2 \to 0^+_3$. However, the calculations with the cluster breaking such as the AMD, FMD, and $3\alpha+p_{3/2}$ show the opposite results. They show the larger $E2$ strength for $2^+_2 \to 0^+_3$ than that for $2^+_2 \to 0^+_2$. This result indicates that the $E2$ strengths between excited cluster states are sensitive to the cluster breaking component. The band assignment for the 2^+_2 has not been experimentally confirmed yet.

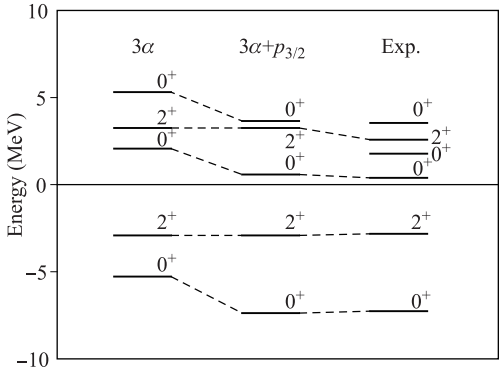

Fig. 4 ^{12}C energy spectra for 0^+ and 2^+ states. The results obtained by the 3α-cluster GCM calculations with and without inclusion of the $p_{3/2}$ configuration are compared. The experimental spectra are also shown. Reproduced from Ref. [60].

Table 1 The comparison of $E2$ transition strengths (e^2fm^4) between 0^+ and 2^+ states calculated with microscopic 3α cluster models (THSR [61], GCM [34], RGM [32, 33], and 3αGCM [60]) and models with 3α breaking ($3\alpha+p_{3/2}$ [60], FMD [46], and AMD [45]). The experimental data are also shown. The table is from Ref. [60].

Transition	Model							Exp.
	THSR	GCM	RGM	3α	$3\alpha+p_{3/2}$	FMD	AMD	
$2^+_1 \to 0^+_1$	9.5	8.0	9.3	10.8	7.4	8.69	8.5	7.6 ± 0.4
$2^+_1 \to 0^+_2$	0.97	0.7	1.1	1.4	5.1	3.83	5.1	2.6 ± 0.4
$2^+_1 \to 0^+_3$				0.4	0.2			
$2^+_2 \to 0^+_1$	2.4		2.5	4.0	1.1		0.4	$1.57^{+0.14}_{-0.11}$
$2^+_2 \to 0^+_2$	295		210	183.3	76.5		102	
$2^+_2 \to 0^+_3$	104			64.4	165.5		311	

3.5 Monopole and dipole excitations in ^{12}C

Isoscalar monopole (ISM) and dipole (ISD) transitions are good probes for cluster states [28, 51, 65–67]. As pointed out by Yamada *et al.*, two different modes of ISM excitations coexist in light nuclei [66]. One is the isoscalar giant monopole resonance (ISGMR), and the other is the cluster mode in relatively lower energy than the ISGMR. The former is associated with the collective vibration, the so-called breathing mode, which is described by coherent 1p-1h excitations. The latter corresponds to the large amplitude mode of inter-cluster motion, which can be directly excited by the ISM operator. It means that the coexistence of mean-field and cluster aspects can be seen also in the ISM excitation phenomena.

The low-energy ISM strengths have been experimentally observed in ^{12}C [63, 68]. In order to clarify the origin of the low-energy ISM strengths separating from the high-energy ISGMR, a hybrid model of the shifted basis AMD (sAMD) combined with the 3α-GCM was applied to ^{12}C [69]. The sAMD is designed to describe coherent 1p-1h excitations on top of the ground state and can describe giant resonances [70]. However it is difficult to describe the large amplitude inter-cluster motion within the sAMD, because the method is based on a small amplitude approximation. To take into account the large amplitude inter-cluster motion, the 3αGCM is combined with the sAMD by explicitly superposing 3α cluster configurations.

The ISM strength functions calculated with the sAMD+3αGCM are shown in Fig. 5. The sAMD+3αGCM calculation including full 3α configurations shows the separation of the low-energy and high-energy parts of the ISM strengths, and is qualitatively consistent with the experimental data. To see contributions of the large amplitude cluster motion to the ISM strengths, we also calculate the ISM strengths within truncated model spaces. Figures 5(e), (d), and (c) show the calculations with only the sAMD bases (without 3α configurations), the vertical 3α configurations ($\theta = \pi/2$) at small distances in addition to the sAMD bases, the vertical 3α configurations ($\theta = \pi/2$) at various distances, respectively. The sAMD describes only the high-energy ISM strengths for the ISGMR but fails to describe the significant low-energy ISM strengths [Fig. 5(e)]. As the 3α configurations added to the sAMD bases are increased, a peak grows up and comes down to the low-energy region [Figs. 5(d) and (c)]. Figure 5(c) for the vertical configurations shows a single peak in the low-energy region but no splitting. Finally, in the full sAMD+3αGCM calculation, where the angular motion of the third α cluster is taken into account, the low-energy strength is split into two peaks for the 0_2^+ and 0_3^+ states because of coupling of distance and rotational motion of cluster positions. The analysis indicates that the large amplitude cluster motion (distance mode) is essential for sum of the low-energy ISM strengths, and then the strength is fragmented by the coupling with the rotational motion of α clusters.

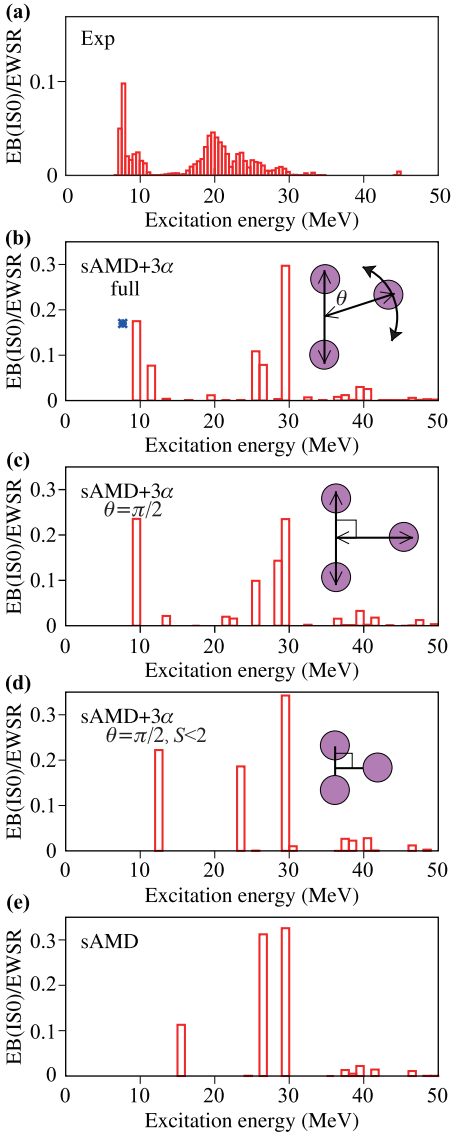

Fig. 5 Energy weighted ISM strength distributions obtained by the sAMD+3αGCM and those measured by (α, α') scattering [63]. The experimental $E0$ strength for the 0_2^+ measured by electron scattering [64] is also shown in panel **(b)**. Panels **(c)** and **(d)** are strengths calculated with truncated model space of 3α configurations: (c) calculation using 3α configurations with the fixed angle $\theta = \pi/2$ in addition to the sAMD bases. (d) same as (c) but only compact 3α configurations with $|\boldsymbol{S}_i| < 2$ fm. **(e)** ISM strengths obtained by only sAMD bases without 3α configurations. Figures (a), (b) (e) are reproduced from Ref. [28].

Let us turn to the ISD excitations in ^{12}C. Significant low-energy ISD strengths have been observed in $E_x = 10$–15 MeV region by α inelastic scattering experiments [63, 68]. The ISD strength functions obtained by the sAMD+3αGCM calculation are shown in Fig. 6. Similarly to the ISM excitations, the calculation shows the low-energy strengths and its decoupling from the high-energy strengths for the ISGDR. In the low-energy region, there are two peaks for the 1_1^- and 1_2^- states. The predicted low-energy strengths are likely to be assigned to the experimentally observed low-energy ISD strengths in this energy region.

The 1_1^- state for the lower peak has a spatially developed 3α cluster structure, whereas the 1_2^- state is dominantly described by a compact structure with no spatial development of clusters. The ISD strengths calculated using truncated model spaces are also shown in Fig. 6. The sAMD calculation without 3α configurations shows only one 1^- state in $E < 20$ MeV, which approximately corresponds to the 1_2^- strength obtained in the full sAMD+GCM calculation. No low-lying cluster state was obtained in the sAMD. When short-distance 3α-cluster configurations are added to the sAMD model space, the ISD strength for the 3α-cluster state appears around 20 MeV [Fig. 6(c)]. In the full sAMD+GCM calculation, the strength for the cluster mode comes down lower than the compact 1_2^- state because of inclusion of large distance cluster configurations. One can see again that the large amplitude inter-cluster motion play a key role in lowering of the cluster modes also in the ISD excitations.

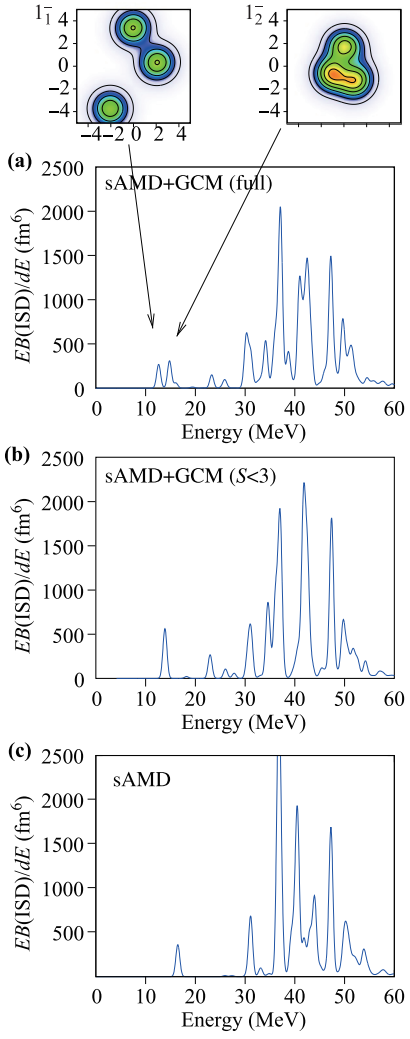

Fig. 6 Energy weighted ISD strength functions calculated with **(a)** the full sAMD+GCM and **(b, c)** calculations using truncated model spaces of configurations: (b) the sAMD with $|\boldsymbol{S}_k| \leq 4$ fm 3α configurations and (c) the sAMD without 3α configurations. Matter density distribution for the dominant configurations of 1_1^- and 1_2^- states is also shown. Reproduced from Ref. [58].

4 Clustering in ^{16}O

4.1 First excited state of the doubly-closed-shell nucleus ^{16}O

^{16}O is the doubly-closed-shell nucleus which is the most fundamental nucleus where the mean-field dynamics should firmly work and we expect the lowest excited states should be one-particle one-hole states with the structure $(0p)^{-1}(0d1s)^1$. These one-particle one-hole states should have negative parity. However, the observed first excited state is of positive parity. It has zero spin $J^\pi = 0^+$ and is located at $E_x = 6.05$ MeV. In the vicinity of the first excited 0_2^+ state we have a negative-parity state with $J^\pi = 3^-$ at 7.13 MeV. This $J^\pi = 3^-$ state is known to have dominantly one-particle one-hole structure and shell-model calculations since early time have all succeeded to reproduce this 3_1^- state [71]. However, as for the 0_2^+ state at 6.05 MeV, no shell model calculation has ever succeeded to reproduce it. In order to have positive-parity states, one has to make at least $2\hbar\omega$ excitation from the closed-shell configuration such as $(0s)^{-1}(1s)^1$, $(0p)^{-1}(1p)^1$, $(0p)^{-2}(1s0d)^2$. Since the magnitude of $\hbar\omega$ around ^{16}O is about 15 MeV, the $2\hbar\omega$ excitation means that the excitation energy is about 30 MeV, which is very large compared with the observed excitation energy, 6.05 MeV. At present, according to shell-model studies and other mean-field-model studies, the 0_2^+ state is considered to have not only $2\hbar\omega$ excited configurations but also $4\hbar\omega$ and even higher excited configurations. These shell-model and mean-field studies therefore admit that even in the doubly-closed-shell nucleus, the mean field is not firmly formed and the first excited 0_2^+ state has a very exotic structure which is largely deviated from the orthodox shell-model picture.

In order to explain the very low excitation energy of the first excited 0_2^+ state, the idea was introduced that the doubly-closed-shell structure of the ground state makes a very large change into a strongly deformed structure of the first excited 0_2^+ state. At first the deformed structure due to two-particle two-hole excitation was studied and then it was extended to the deformed structure due to four-particle four-hole excitation [72]. While the deformed four-particle four-hole structure of Ref. [72] was based on the strong coupling of four-particle configuration with the four-hole configuration so as to form a single deformed mean field of the total nucleus as in the usual deformed-mean-field model, Arima, Horiuchi, and Sebe proposed the weak coupling model of four-particle configuration with the four-hole configuration [3]. When the coupling between particles and holes is weak, the 4 $0p$-holes take the configuration similar to the ground state of ^{12}C and the 4 $1s0d$-particles take the configuration similar to the ground rotational band of ^{20}Ne:

$$\Psi(K^\pi = 0_1^+, J) = |(0p)^{-4}(^{12}\mathrm{C}, 0^+), (1s0d)^4(^{20}\mathrm{Ne}, J^+)\rangle. \tag{8}$$

The configuration of 4 $1s0d$-particles of ground rotational band states of ^{20}Ne is well approximated by the SU(3) configuration with the symmetry $(\lambda, \mu) = (8, 0)$. According to the Bayman-Bohr theorem [2], this SU(3) state is just equivalent to the cluster state of ^{16}O+α structure:

$$|(0s)^4, (0p)^{12}, (1s, 0d)^4; (8, 0)J\rangle$$

$$= C_J \mathcal{A}\{R_{8,J}\left(r_{O-\alpha}, \frac{16}{5}\nu\right) Y_J(\hat{r}_{O-\alpha})\phi(\alpha)\phi(^{16}O)\} \times g(\vec{X}_G, 20\nu). \quad (9)$$

Thus the weak-coupling model wave function has a relation to the ^{12}C+α cluster wave function. The energy of the state $\Psi(K^\pi = 0_1^+, J = 0)$ was estimated by using the observed excitation energy of the low-lying $1/2^-$ state of ^{19}F which was regarded to have the structure $|p_{1/2}^{-1}\,(1s0d)^4(^{20}\mathrm{Ne}, 0^+) : J = 1/2\rangle$. The estimated excitation energy of $\Psi(K^\pi = 0_1^+, J = 0)$ is about 6 MeV which is very close to the observed excitation energy $E_x = 6.05$ MeV.

4.2 Clustering in ^{16}O with cluster approaches: ^{12}C+α and 4α structures

In order to understand low-lying energy spectra of ^{16}O, the tetrahedral 4α-cluster structure has been discussed for a long time in relation with the T_d symmetry [5, 6, 79–82]. The tetrahedral 4α configuration constructs a rotational band of 0^+, 3^-, 4^+, $\cdots$ states. The ground and 3_1^- (6.13 MeV) states have been assigned to the T_d-invariant 4α band, but the assignment of the 4^+ state in the tetrahedral 4α band has not been confirmed yet.

In addition to the tetrahedral 4α structure, $^{12}\mathrm{C} + \alpha$ cluster states have been suggested [38]. The excited states assigned for the $^{12}\mathrm{C} + \alpha$ cluster states are classified into the parity doublet $K^\pi = 0^+$ and $K^\pi = 0^-$ bands: the 0_2^+ (6.06 MeV), 2_1^+ (6.92 MeV), 4_1^+ (10.36 MeV), and 6_2^+ (16.23 MeV) in the $K^\pi = 0^+$ band, and the 1_2^- (9.59 MeV), 3_2^- (11.60 MeV), and 5_1^- (14.66 MeV) in the $K^\pi = 0^-$ band. These assignments are consistent with the observed α-transfer and α-decay properties and also theoretical calculations with cluster models (see for example, Refs. [75, 84] and references therein).

In order to investigate cluster structures of ^{16}O, microscopic and semi-microscopic cluster models have been applied since 1970s [24, 66, 70, 74, 75, 79, 80, 85–91]. More recently, the semi-microscopic 4α calculation by Funaki *et al.* predicted a 4α cluster gas state near the 4α threshold energy [74, 90]. The semi-microscopic 4α calculation describes not only the 4α cluster gas but also ^{12}C+α states below the gas state. Experimental search for the 4α cluster gas state in excited states of ^{16}O has been performed [77].

The $^{12}\mathrm{C}(0_1^+) + \alpha$ band in ^{16}O was obtained also by microscopic $^{12}\mathrm{C}(0_2^+)$+α cluster models, but its excitation energy was much overestimated by a factor 2 of 3 in the calculation with the microscopic cluster model. In addition, another problem is left: how α clusters are formed in 16-nucleon dynamics?

The AMD+VAP method has been applied to ^{16}O [15, 17, 92, 93]. In the result, the tetrahedral 4α-cluster and ^{12}C+α-cluster structures are obtained in a fully microscopic way based on nucleon degrees of freedom without assuming existence of clusters [73]. Detailed cluster structures in highly excited states have been investigated by the ^{12}C(AMD)+αGCM calculation [78] and that combined with the AMD+VAP [73].

Figure 7 shows the energy spectra obtained by the AMD+VAP combined with the ^{12}C(AMD)+αGCM. Matter density distributions in the dominant components are also shown. The calculation reasonably reproduces the experimental energy spectra. For the ground band, the 0_1^+, 3_1^-, and 4_2^+ states are assigned as members of the tetrahedral band consistently with the discussion of α-transfer properties in Ref. [82]. The $^{12}\mathrm{C}+\alpha$ cluster structure can be seen in the 0_2^+, 2_1^+, 4_1^+, 1_2^-, 3_2^-, and 5_1^- states, which construct the parity-doublet bands, $K^\pi = 0^+$ and $K^\pi = 0^+$ as suggested in Ref. [83]. It should be noted that the ordering of two 4^+ states for the $^{12}\mathrm{C} + \alpha$ and tetrahedral 4^+ states is opposite between the AMD+VAP calculation with and without the $^{12}\mathrm{C} + \alpha$ cluster configurations. It turns out that the detailed cluster dynamics such as the ^{12}C-α relative motion and rotation of the deformed ^{12}C-cluster are essential to lower the $^{12}\mathrm{C} + \alpha$ band.

The occupation probability of oscillator quanta N shells in the harmonic oscillator basis expansion is shown in Fig. 8. One can see that the occupation probability for the $^{12}\mathrm{C} + \alpha$ cluster states is distributed widely in the higher oscillator region because of the spatially developed $^{12}\mathrm{C} + \alpha$ cluster structure. The 0_1^+ and 3_1^- states in the tetrahedral band contain significant $N = 12$ and $N = 13$ shell components corresponding to $0p0h$ and $1p1h$ configurations, respectively. It indicates that these two states can be roughly interpreted, at least at the leading order, as the lowest shell configurations on the doubly closed p shell. However, one can see that these tetrahedral band states also contain significant components of higher shell configurations because of the cluster correlation originating in finite size 4α configurations. The result shows the importance of the cluster aspects in ^{16}O: the cluster correlations in the ground band and the $^{12}\mathrm{C} + \alpha$ cluster structure in the excited band.

In highly excited states above the 0_2^+ state, various kinds of cluster structures have been predicted by semi-microscopic $^{12}\mathrm{C} + \alpha$OCM and 4αOCM calculations [66, 74, 75, 89, 90]. The microscopic calculation of the $^{12}\mathrm{C(VAP)} + \alpha$GCM obtained the higher nodal $^{12}\mathrm{C}(0_1^+)$+α, the $^{12}\mathrm{C}(2_1^+)$+α, and the $^{12}\mathrm{C}(0_2^+)$+α structures in the 0_3^+, 0_4^+, and 0_5^+ states. In Fig. 9, the 0^+ spectra calculated with the $^{12}\mathrm{C(VAP)} + \alpha$GCM are shown in comparison with the $^{12}\mathrm{C} + \alpha$OCM and 4αOCM calculations. The microscopic calculation ($^{12}\mathrm{C(VAP)} + \alpha$GCM) supports the cluster structures predicted by the semi-microscopic calculations, though the detailed ordering of

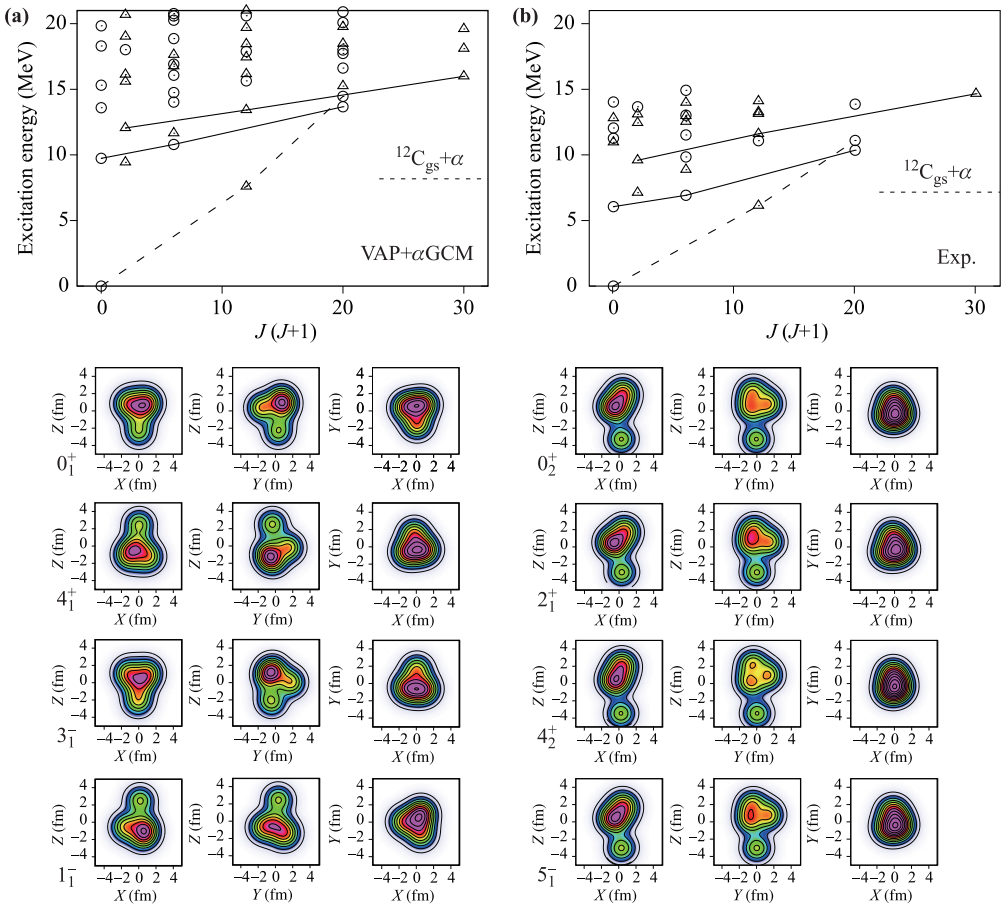

Fig. 7 Top: Energy levels of ^{16}O calculated by the VAP+αGCM **(a)** and the experimental data **(b)**. Positive- and negative-parity levels are shown by circles and triangles, respectively. The ground and $^{12}\mathrm{C}+\alpha$ bands are connected by dashed and solid lines, respectively. Bottom: Density distributions in the intrinsic states obtained by the VAP. (In the VAP+αGCM calculation, the 4^+_2 state obtained in the VAP comes down lower than the 4^+_1 of the VAP.) The densities integrated along the Y, X, and Z axes are plotted on the (left) X–Z, (middle) Y–Z, and (right) X–Y planes, respectively. Reproduced from Ref. [73].

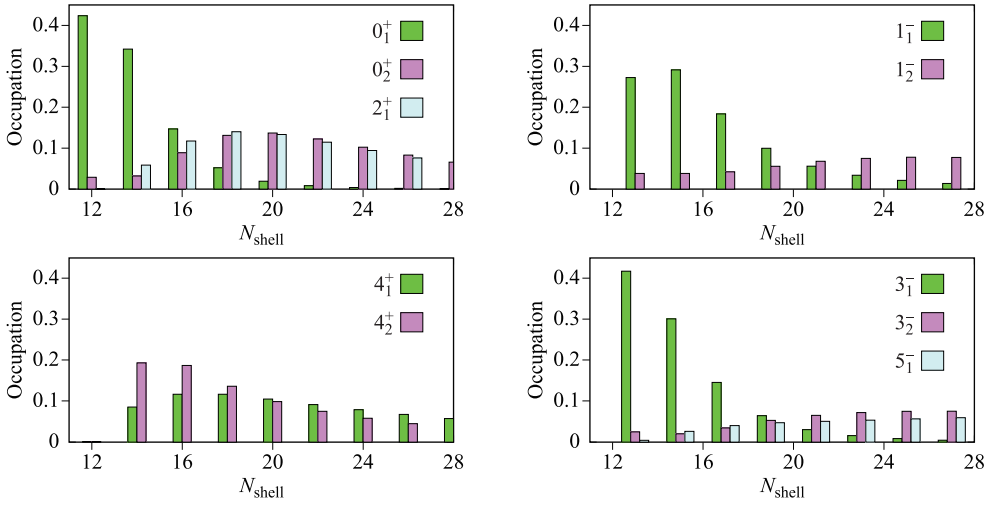

Fig. 8 Occupation probability of N shells in the harmonic oscillator shell-model expansion for ^{16}O obtained by the VAP+αGCM. Reproduced from Ref. [73].

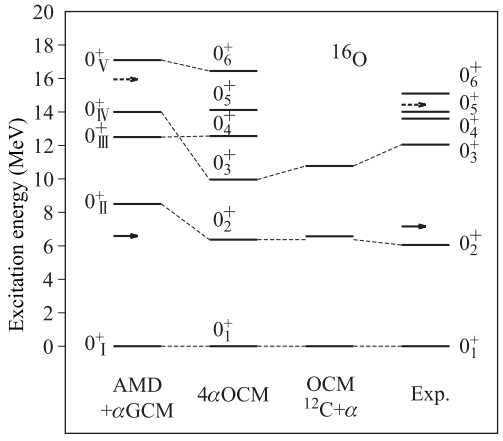

Fig. 9 Excitation energies of 0^+ states in ^{16}O calculated with the present ^{12}C(AMD)+αGCM (AMD+αGCM) and those of the 4α-OCM and ^{12}C+α-OCM from Refs. [74, 75]. Experimental energy levels of 0^+ states are taken from Refs. [76, 77]. ^{12}C(0^+_1)+α and ^{12}C(0^+_2)+α threshold energies are plotted by solid and dashed arrows, respectively. Reproduced from Ref. [78].

the cluster states are not consistent between two calculations, ^{12}C(VAP) + αGCM and 4αOCM calculations.

4.3 Monopole excitations in ^{16}O

As discussed in the previous section, the ISM excitation is a good probe for cluster states. Indeed, the low-energy ISM strengths are described well by the 4αOCM calculation [66]. But such the cluster model is not enough to describe the high-energy ISM strengths for the ISGMR. The ^{12}C(AMD)+αGCM combined with the sAMD describes the low-energy ISM strengths for cluster states and also the high-energy strengths for the ISGMR (see Fig. 10). The success in describing two different ISM modes, the low-energy cluster mode and high-energy ISGMR mode, owes to the large model space containing cluster structures in the ^{12}C(AMD)+α basis wave functions and 1p-1h excitations in the sAMD basis wave functions. The ISM strengths obtained by the sAMD calculation without the cluster configurations are also shown in Fig. 10. In the sAMD calculation, there is no low-energy ISM strengths because the sAMD model space contains only small amplitude modes but not the large amplitude cluster motion. On the other hand, the full calculation of the ^{12}C(AMD)+αGCM combined with the sAMD shows the significant low-energy ISM strengths for the cluster states in $E_x \lesssim 15$ MeV, which are decoupled from the ISGMR strengths in the higher-energy region. The result clearly shows that the large amplitude cluster motion gives essential contributions to the low-energy ISM strengths in ^{16}O. This situation is similar to the case of ^{12}C. It is worth to mention that, this calculation is the

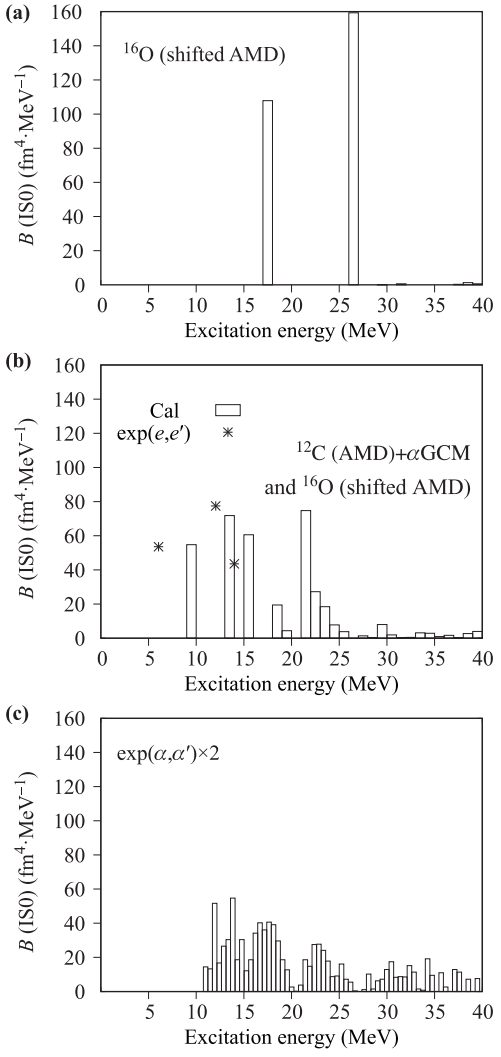

Fig. 10 ISM transition strength functions. The theoretical B(ISM) calculated with **(a)** the ^{16}O (shifted AMD), **(b)** full calculation of the ^{12}C (AMD)+αGCM combined with ^{16}O (shifted AMD), and **(c)** the experimental data measured by (α, α') scattering. The experimental B(ISM) (fm^4) converted from $B(E0)$ measured by (e, e') scattering for the 0^+ states at 6.05, 12.05, and 14.01 MeV are also shown by stars in the middle panel. The data from Ref. [94] are multiplied by a factor 2 in the bottom panel. Reproduced from Ref. [78].

first microscopic calculation that describes the coexistence of two different ISM modes (the low-energy cluster and high-energy GMR modes) in a unified manner.

5 Clustering in ^{20}Ne

5.1 Four-body correlation at surface on ^{16}O

As mentioned previously, the shell model studies of ^{20}Ne showed that the main configuration of the

ground band states is given by the SU(3) states $|(0s)^4,(0p)^{12},(1s0d)^4;(8,0)J\rangle$ [95, 96]. Since these SU(3) states are equivalent to the ^{16}O+α cluster states, the ground band satates of ^{20}Ne are typical example of the ground state and its rotational member states which possess strong α-clustering character. Except very light nuclei like ^{8}Be, the strong clustering feature is not expected to show up in the ground state and its rotational member states. Therefore the study of the clustering feature of the ground band of ^{20}Ne is very important. Tomoda and Arima [97] made an extensive study of this problem. They performed the study by hybridizing the $(1s0d)^4$ shell model and microscopic ^{16}O+α cluster model. They adopted a microscopic Hamiltonian which involves a two-body effective interaction consisting of central, L-S and Coulomb potentials. The states below the α-decay threshold were obtained by diagonalizing the Hamiltonian, while for those above the threshold, the α–^{16}O scattering phase shifts were calculated by solving a coupled scattering equation variationally under an appropriate boundary condition. Energy levels, reduced α-widths, and B(E2) values were calculated and compared with experimental values. Three $K^\pi = 0^+$ bands built on 0^+_1 (g.s.), 0^+_2 (6.72 MeV) and 0^+_4 (8.6 MeV) states and the first $K^\pi = 0^-$ band on the 1^-_1 state at 5.79 MeV were successfully described by the model. It was found that the wave functions of the ground band members consist mainly of the (80) components. However, it was found that small admixtures of cluster components $(\lambda,0)$ with λ larger than eight, which do not affect the α-spectroscopic factors very much, are necessary to reproduce the observed α-widths of the 6^+ and 8^+ members and also the B(E2) strengths between the ground band members and the quadrupole moment of the 2^+ state with an effective charge $\delta e = 0.15e$, which is much smaller than that required in the ordinary shell model

5.2 Cluster structures in ^{20}Ne studied with AMD

5.2.1 Nucleon spin alignment

As was explained, the AMD method is suited for studying the coexistence and interplay of the shell-model feature and cluster-model feature. The first study of ^{20}Ne with AMD was reported in Ref. [98] in which structure of the yrast line states of ^{20}Ne was studied with AMD by constructing the rotating intrinsic states. The construction was made by the frictional cooling method under the constraint that the expectation value of the angular momentum vector takes the given value in its magnitude while its direction is determined variationally. Namely when the expectation values of angular momentum operators J^{op}_k, $(k = x \sim z)$ by AMD wave function are denoted as $\langle J^{op}_k\rangle$, the magnitude of $\sum_k \langle J^{op}_k\rangle\langle J^{op}_k\rangle$ is constrained to take given values. Unlike the ordinary approach with the cranking method, angular momentum projection was applied to these rotating intrinsic states in order to get good angular momentum states. Two-body spin-orbit force was adopted and nucleon spin orientations were determined by energy variation, which enabled us to describe the dissolution of clusters more satisfactorily. It was found that for both positive and negative parity low spin states, the two-cluster structure of ^{16}O+α resulted as a predominant configuration, and that the ^{16}O+α clustering becomes weaker as the spin goes up and mixes with the spin-aligned oblate structure when going from 6^+ to 8^+.

5.2.2 Dissolution and formation of α clustering

In Ref. [83], it was proposed that the ground rotational band and the $K^\pi = 0^-$ rotational band upon $J^\pi = 1^-$ level at 5.78 MeV constitute an inversion doublet which comes from the parity-violating ^{16}O+α intrinsic structure. However it was also discussed that the α clustering in the ground band is weaker than that in the $K^\pi = 0^-$ band whose clustering is quite prominent. The quantitative study about how much weak the α clustering in the ground band is important for our understanding of the coexistence and interplay of the shell-model (mean-field) dynamics and cluster dynamics. The discussion of this problem can be made much clearer by comparing it with the same problem of ^{40}Ca+α clustering in ^{44}Ti. In ^{44}Ti, we have the $K^\pi = 0^-$ rotational band (upon $J^\pi = 1^-$ level at 7.0 MeV) which is discovered by α-transfer reaction (Ref. [99] and references therein) and is regarded as constituting an inversion doublet together with the ground band that comes from the parity-violating ^{40}Ca+α intrinsic structure. We compare the results of the AMD calculation of ^{20}Ne [26] with those of the AMD calculation of ^{44}Ti [44] both of which are obtained by the use of the Gogny D1S interaction as the effective nuclear force. The intrinsic wave function of the ground state obtained by AMD does not show density distribution of ^{16}O+α clustering for ^{20}Ne and also the AMD intrinsic wave function of the ground state does not show density distribution of ^{40}Ca+α clustering for ^{44}Ti. On the other hand, the density distribution of the AMD intrinsic wave function of the $J^\pi = 1^-$ state of the $K^\pi = 0^-$ band shows clearly density distribution of prominent ^{16}O+α clustering in ^{20}Ne and also that of ^{40}Ca+α clustering in ^{44}Ti. Although the density distribution of the ground state does not show ^{16}O+α clustering, the component of ^{16}O+α cluster wave function contained in the ground state wave function has the squared amplitude of 70%, which is due to the duality property of the shell-model wavefunction, $|(0s)^4(0p)^{12}(1s0d)^4;[44444](\lambda,\mu) = (8;0);J = 0\rangle$.

Table 2 shows the results of the AMD calculation of Ref. [26] where we see the properties of the calculated lev-

Table 2 Squared amplitude of the ^{16}O+α component W^J and the expectation value of the two-body spin-orbit interaction $\langle \widehat{V}_{ls} \rangle$ (in MeV) for each state of the inversion-doublet rotational bands of ^{20}Ne obtained by AMD calculation [26].

$K^\pi = 0^+$	J^π	W^J	$\langle \widehat{V}_{ls} \rangle$	$K^\pi = 0^-$	J^π	W^J	$\langle \widehat{V}_{ls} \rangle$
	0^+	0.70	−5.2		1^-	0.95	−0.8
	2^+	0.68	−5.3		3^-	0.93	−0.8
	4^+	0.54	−5.9		5^-	0.88	−0.7
	6^+	0.34	−8.4		7^-	0.71	−0.9
	8^+	0.28	−10.9		9^-	0.70	−1.3

els of the inversion-doublet bands of ^{20}Ne. The squared amplitude of the ^{16}O+α clustering component W^J in the ground band decreases rather rapidly as the spin value J increases from 70% of the 0^+ state to 28% of the 8^+ state. This decrease of the cluster character is reflected in the increase of the nucleon-spin alignment for larger J [98] discussed above. It can be seen in the increase of the expectation value of the two-body spin-orbit interaction $\langle \widehat{V}_{ls} \rangle$ for larger J. This feature of the spin-alignment well reflects the mean-field-type character of the ground bend of ^{20}Ne. On the other hand, in the $K^\pi = 0^-$ band, the W^J value of the 1^- state is as large as 95% and the smallest value of W^J for the 9^- state is still as large as 70%. This result means that the $K^\pi = 0^-$ band has prominent clustering character of ^{16}O+α. It is supported by the small expectation values $\langle \widehat{V}_{ls} \rangle$ for all the states of the $K^\pi = 0^-$ band.

In the case of ^{44}Ti, just like the ^{20}Ne case, there exists inversion-doublet bands composed of the ground rotational band and the $K^\pi = 0^-$ band built upon the $J^\pi = 1^-$ at 7.0 MeV. The negative-parity band levels were found by the α-transfer reaction [99]. In Table 3, we show the squared amplitude of the ^{40}Ca+α component W^J of each level of the inversion-doublet bands of ^{44}Ti obtained by the AMD study of Ref. [100]. We see that the ^{40}Ca+α clustering component is very small in the ground band. Even the largest clustering percentage for the ground 0^+ state is 40%, which means that non-clustering component is 60% for the ground state. The 10^+ and 12^+ states have almost no clustering component. As for the $K^\pi = 0^-$ band, the largest clustering percentage is 56% for the 1^- state, which is fairly smaller than 95% of the 1^- state of ^{20}Ne. The small clustering component in the inversion doublet bands is considered to be due to the strong spin-orbit potential and also to the strong attraction from the ^{40}Ca core nucleus. Although the ^{40}Ca+α percentage of the ground band is not larger than 40%, the AMD calculation does not show the existence of $J^\pi = 0^+$ excited state whose ^{40}Ca+α component is larger than 40% and has relative-motion nodal number $n_r = 6$. Here the relative-motion nodal number n_r means the nodal number of the reduced width amplitude $\mathcal{Y}(r)$ defined as

$$\mathcal{Y}(r) = r\langle \frac{\delta(r_{rel} - r)}{r^2} Y_{0.0}(\widehat{r}_{rel}) \phi(^{40}\mathrm{Ca}) \phi(\alpha) | \Phi^{\mathrm{AMD}} \rangle. \quad (10)$$

The relative-motion nodal number $n_r = 6$ is the smallest nodal number of $\mathcal{Y}(r)$ which is allowed by the inter-cluster Pauli principle. The value of n_r of the $J^\pi = 1^-$ of the $K^\pi = 0^-$ band is also $n_r = 6$. The fact that the percentage of ^{40}Ca+α component of the ground state is 40% means that the percentage of the SU(3) shell-model component $\Phi^{(12,0)} = |^{40}\mathrm{Ca\text{-}core},\ (1p0f)^4; [4^{10}](\lambda, \mu) = (12, 0)\rangle$ is less than 40% because $\Phi^{(12,0)}$ has the duality property that it is equivalent the cluster-model wave function of ^{40}Ca+α. The decrease of the shell-model component with good spatial and SU(3) symmetry seen in the ^{44}Ti ground state is considered to be more pronounced in the ground states of heavier nuclei.

Table 3 Squared amplitude of the ^{40}Ca+α component W^J for each state of the inversion-doublet rotational bands of ^{44}Ti obtained by AMD calculation [100].

$K^\pi = 0^+$	J^π	0^+	2^+	4^+	6^+	8^+	10^+	12^+
	W^J	0.39	0.34	0.32	0.25	0.21	0.06	0.06
$K^\pi = 0^-$	J^π	1^-	3^-	5^-	7^-	9^-		
	W^J	0.56	0.50	0.43	0.38	0.32		

6 Clustering in neutron-rich nuclei

6.1 Overview

In experimental and theoretical studies of unstable nuclei in the past decades, a variety of cluster states have been discovered also in unstable nuclei as well as stable nuclei. In neutron-rich nuclei, it has been revealed that excess neutrons play important roles in the cluster states such as cluster weakening and enhancement. A question is what happens when additional neutrons are appended to the prominent cluster structures of stable nuclei. For instance, evolution of the 2α, 3α, and ^{16}O+α cluster structures in Be, C, and Ne isotopes in the presence of surrounding valence neutrons has been discussed by many groups (Ref. [106] and references therein).

Fascinating cluster aspects of neutron-rich nuclei can be seen even in the ground states because of the valence neutrons. Structures of the ground states vary depending on proton and neutron numbers. Figure 11 shows a sketch of the structure variation with the increase of the neutron number N in light nuclei. Stable nuclei with $Z = N = 2n$ show $n\alpha$ cluster structures such as the 2α and 3α clustering in ^{8}Be and ^{12}C. In Be isotopes, the cluster structure in the ground states rapidly changes

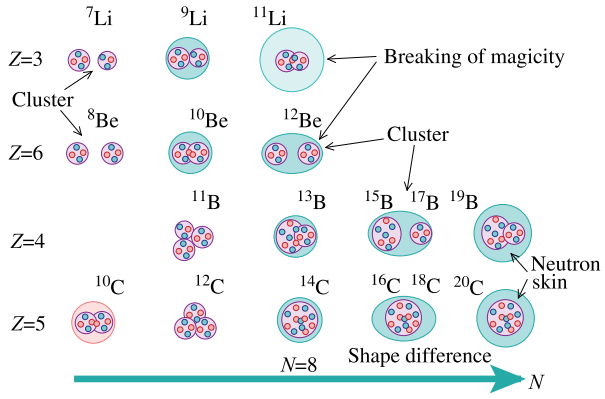

Fig. 11 Schematic figures for structure changes in the ground states of neutron-rich Li, Be, B, and C isotopes. Reproduced from Ref. [101].

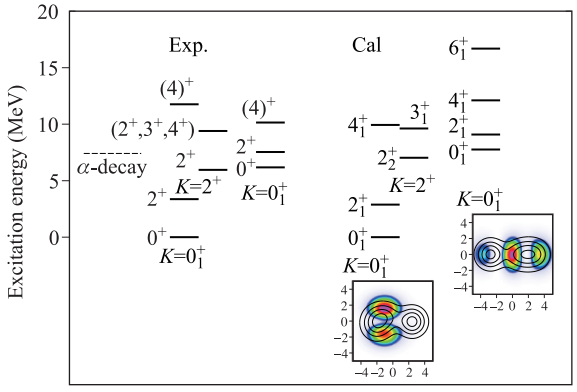

Fig. 12 Energy spectra for positive-parity states of ^{10}Be obtained by the AMD+VAP using the MV1 force are shown together with experimental data. Matter density and valence neutron density in ^{10}Be($0^+_{1,2}$) are shown by contour and color mapping, respectively. Reproduced from Ref. [102].

along the isotope chain. The ground state of ^{8}Be is a quasi-bound state of two α particles. As extra neutrons are added, the remarkable 2α structure weakens in ^{10}Be, and it develops again in ^{12}Be. Consequently, the ^{12}Be ground state is a largely deformed state with the dominant intruder configuration even though it is a $N = 8$ nucleus. This phenomenon is known to be breaking of the neutron magic number in neutron-rich Be. By contrast, the ground states in neutron-rich C isotopes do not show cluster development, but generally have weak cluster structures with an oblately deformed proton structure distributed in a compact region. It means that 3α cluster structure formed in ^{12}C is quenched by excess neutrons around the 3α cluster.

In excited states of neutron-rich nuclei, further remarkable cluster aspects can be seen. An example is molecular orbital structures in Be isotopes. In ^{10}Be(0^+_2), two valence neutrons occupy the longitudinal molecular orbital (MO) called the σ-orbital around the 2α. The σ-orbital neutrons bond two α clusters at a certain interval between two αs. The largely deformed intrinsic structure is stabilized by this bonding mechanism of the valence neutrons, and constructs the rotational $K^\pi = 0^+_2$ band in ^{10}Be spectra (see Fig. 12). In addition to the MO σ-bond structure, dinuclear cluster resonances composed of ^{6}He and α clusters have been recently suggested in highly excited states above the ^{10}Be(0^+_2) state. An important difference between the MO σ-bond structure and the dinuclear cluster resonances is the valence neutron configuration. In the MO σ-bond structure, valence neutrons are moving in the molecular orbital around in the whole system bonding two α clusters. However, in the cluster resonances, a ^{6}He cluster is formed by valence neutrons moving in the atomic-like orbital around one of α clusters. Also in neutron-rich *sd*-shell nuclei such as ^{22}Ne, similar cluster structures, the MO σ-bond structure and dinuclear resonances, have been predicted. In in ^{22}Ne, the ^{16}O+α core is formed in excited states. There, MO σ-bond structures with σ-orbital neutrons around the ^{16}O+α core and also ^{18}O+α dinuclear resonances have been proposed [106–108].

One can expect further fascinating cluster phenomena in neutron-rich nuclei such as $n\alpha$ cluster structures with valence neutrons. For instance, in excited states of neutron-rich C, a linear-chain 3α-cluster structure with valence neutrons has been predicted theoretically [109]. Very recently, candidate states for this prediction of the linear-chain state have been observed experimentally [110, 111]. These facts indicate appearance of various types of cluster structures in the ground and excited states of neutron-rich nuclei. Searching for new cluster structures is being performed extensively in experimental studies for various unstable nuclei as well as theoretical studies.

6.2 Cluster structures in Be isotopes

6.2.1 Molecular orbital structures and cluster resonances

Cluster structures of neutron-rich Be isotopes have been intensively investigated from both the theoretical and experimental sides [17, 106]. In the observed spectra of ^{10}Be, positive-parity states are classified into the ground, side ($K^\pi = 2^+$), and excited ($K^\pi = 0^+_2$) bands (see Fig. 12). Spectra of ^{10}Be are described well by the AMD+VAP calculation [102]. It should be stressed that formation of two α clusters in 10-nucleon dynamics of ^{10}Be can be seen in the ground and excited states with the AMD framework, which does not rely on the assumption of the α cluster formation but treats all nucleons independently as localized Gaussian wave packets. Distributions of matter and valence neutron densities in

the $K^\pi = 0_1^+$ and $K^\pi = 0_2^+$ bands are shown together with the experimental and calculated energy spectra in Fig. 12. In excited states, the remarkable $2\alpha+2n$ cluster structure is obtained and forms the $K^\pi = 0_2^+$ band starting from the 0_2^+ state. The density distribution of valence neutrons in the 0_2^+ state shows the two-node structure along the 2α direction corresponding to the MO σ orbital. In the experimental spectra, the 2^+ state at 7.54 MeV and 4^+ state at 10.2 MeV are tentatively assigned as the $K^\pi = 0_2^+$ band members [112, 113].

In order to understand the cluster structures of low-lying states of neutron-rich Be isotopes, the molecular orbit (MO) structure, which has been originally proposed for ^{9}Be [114], has been extended to neutron-rich Be isotopes [106, 115–117]. (See Figs. 13 and 14 for sketch of cluster structures in neutron-rich Be.) In the MO picture, valence neutrons in a $2\alpha+Xn$ system occupy molecular orbitals around the 2α, which are described by linear combination of (atomic-like) p-orbits around α clusters in analogy to covalent bonding orbitals. Schematic figures of molecular orbitals are shown in Fig. 14. The lowest nodal MOs are negative-parity orbitals called "$\pi_{3/2}$-orbital" and "$\pi_{1/2}$-orbital". They are ls-favored and ls-unfavored orbitals correspond to the $p_{3/2}$ and $p_{1/2}$ orbits in the spherical shell model limit, respectively. The lowest positive-parity MO denoted by "$\sigma_{1/2}$-orbital" is the longitudinal orbital having two nodes along the α-α direction. It has the nodal structure in the α-α direction direction and therefore it gains the kinetic energy when the α-α distance is stretched. As a result, valence neutrons in the $\sigma_{1/2}$-orbital enhance the cluster structure. However, those in the $\pi_{3/2,1/2}$-orbitals suppress the cluster structure of neutron-rich Be to gain the potential energy. Moreover, the cluster development even changes ordering of single-particle energies of the MOs because of the kinetic energy gain of the $\sigma_{1/2}$-orbital. Namely, the $\sigma_{1/2}$-orbital comes down to the energy lower than the ls-unfavored $\pi_{1/2}$ orbital in the stretched 2α system.

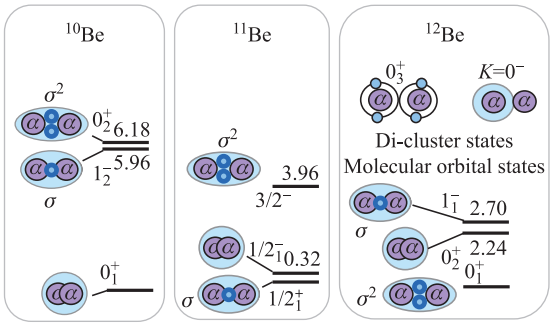

Fig. 13 Schematic figures for cluster structures in ^{10}Be, ^{11}Be, and ^{12}Be. For the molecular-orbital states, the 2α core with the σ-orbital neutrons are illustrated. Experimental values of excitation energies are also shown. Reproduced from Ref. [17].

As a result of the inversion between the $\pi_{1/2}$- and $\sigma_{1/2}$-orbitals in the developed cluster system, the intruder states with large deformation become the ground states of ^{11}Be and ^{12}Be. The assignment of MO configurations to observed band-head states of ^{10}Be, ^{11}Be, and ^{12}Be are illustrated in Fig. 13. Cluster-model and AMD calculations obtain remarkable cluster structures, in particular, for the states having σ-orbital neutrons. The momentum inertia deduced from the observed level spacing between band members supports the theoretical prediction of the developed cluster structures. An example is the energy spectra of the $K^\pi = 0_2^+$ band assigned to the σ^2 configuration in ^{10}Be (see Fig. 12).

6.2.2 N dependence of proton radii

In the ground states of Be isotopes, the weakening and enhancement of cluster structures occur depending on the neutron number as discussed previously. The cluster structure change is induced by change of neutron structure. Namely, the neutron deformation is smallest at $N = 6$ for ^{10}Be, whereas it increases in ^{11}Be and ^{12}Be.

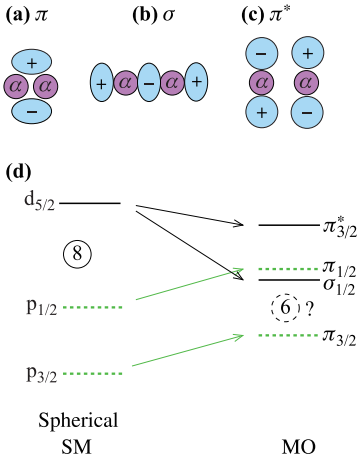

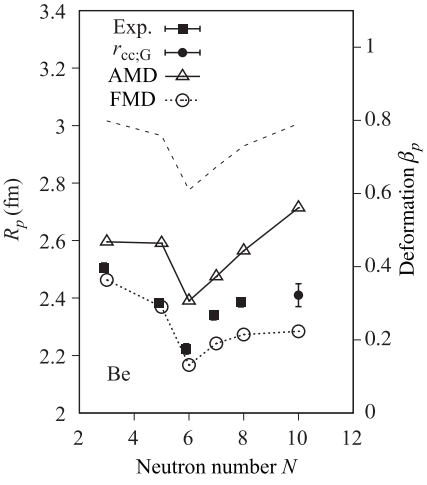

Fig. 14 Left: **(a, b, c)** Sketches of molecular orbitals around the 2α core in neutron-rich Be. **(d)** Sketch of single-particle spectra for valence neutrons of spherical shell-model orbitals and those of molecular orbitals. Right: Radius (R_p) and deformation parameter (β_p) of proton distribution in Be isotopes. The theoretical values calculated by the AMD+VAP using the MV1 force are shown together with the experimental data [103, 104] and the FMD results [104]. Reproduced from Ref. [105].

Reflecting this neutron deformation, the proton deformation β_p shows the similar N dependence; the proton deformation is smallest not at $N = 8$ but at $N = 6$ for ^{10}Be. The deformation change is nothing but the change of cluster structure caused by added neutrons, and can be easily understood by the MO configuration. The cluster structure is weakest in ^{10}Be because of the attractive role of $p_{3/2}$-orbital neutrons, where as it is enhanced in ^{12}Be by the bonding mechanism of σ-orbital neutrons.

How one can experimentally observe the cluster structure change with increase of N in a series of isotopes? N dependence of charge radii can be a good probe to figure out the clustering, because it reflects the change of clustering through the change of proton density distribution. Recently, systematic data of charge radii for unstable nuclei became available. For neutron-rich Be isotopes, charge radii up to ^{12}Be have been precisely measured by means of isotope shift [103, 104]. Figure 14 shows the calculated proton radii of Be obtained by the AMD+VAP calculation and experimental values reduced from the observed charge radii. The proton radius of ^{9}Be is relatively large in Be isotopes because of the remarkably enhanced cluster structure, whereas it decreases at $N = 6$ for ^{10}Be and increases again in the $N > 6$ region for ^{11}Be and ^{12}Be. The systematics of the proton radii reflect the reduction and enhancement of the cluster structure rather directly. The N dependence of the calculated proton radii is consistent with the experimental data. The increase of the proton radius in ^{12}Be is an indirect evidence of the $N = 8$ shell breaking as pointed out in Ref. [104]. The minimum of proton radii at $N = 6$ instead of $N = 8$ can be interpreted as appearance of a new magic number at $N = 6$. The migration of the neutron magic number from $N = 8$ to $N = 6$ can be understood by the change from the single-particle spectra of the spherical shell model to those of the MO in the deformed cluster state as shown in the left panels of Fig. 14.

The systematics of point-proton radii provides useful information for cluster structure change of the ground states along a series of isotopes. Nowadays, systematic data of proton radii for neutron-rich nuclei are available by means of charge changing reactions based on Glauber analysis. The AMD prediction of enhanced cluster structures in neutron-rich B and weak clustering in neutron-rich C will be tested by such experimental measurements of proton radii by charge changing reactions in near future.

6.2.3 Isovector dipole excitations in ^{9,10}Be

Isovector (IV) low-energy dipole (LED) excitations is one of the current issues concerning exotic excitation modes in neutron-rich nuclei. In neutron-rich nuclei, the mode of valence neutron oscillation against a core nucleus is expected to contribute to the IVLED strengths. On the other hand, the normal collective mode of the opposite oscillation between protons and neutrons produces the IV giant dipole resonance (IVGDR). In neutron-rich Be, a variety of dipole excitations may be possible because of excess neutron motions on top of the ground states with the cluster structures. Questions to be answered are whether LED resonances appear and how the GDR is affected in the presence of excess neutrons.

The IV and IS dipole excitations in ^{9}Be and ^{10}Be have been investigated using the sAMD+GCM [29]. The IV dipole ($E1$) strengths for $^{8}\mathrm{Be}(0^+_1) \to {}^{8}\mathrm{Be}(1^-)$, $^{9}\mathrm{Be}(3/2^-_1) \to {}^{9}\mathrm{Be}(1/2^+, 3/2^+, 5/2^+)$, and $^{10}\mathrm{Be}(0^+_1) \to {}^{10}\mathrm{Be}(1^-)$ calculated by the sAMD are shown in Figs. 15(a)–(c). The comparison of the calculation with the experimental photonuclear cross sections for ^{9}Be is shown in Fig. 15(d).

The calculated IVGDR in ^{8}Be shows a two peak structure as expected from the 2α cluster structure with a prolate deformation. The lower peak at $E = 20$–25 MeV is contributed by the longitudinal mode, whereas the higher peak around $E = 30$ MeV is attributed by the transverse mode of the 2α cluster. In ^{9}Be and ^{10}Be, the strengths in the $E > 20$ MeV region correspond to the IVGDR strengths, which are contributed by the IV dipole strengths in the 2α core part. Roughly speaking, the strengths in this energy region of ^{9}Be and ^{10}Be also show two peak structures because of the prolately deformed core. However, compared with the IVGDR strengths in ^{8}Be, the higher peak somewhat broadens in ^{9}Be and it is highly fragmented in ^{10}Be because the transverse mode of the core is strongly influenced by excess neutrons sitting in the transverse direction of the

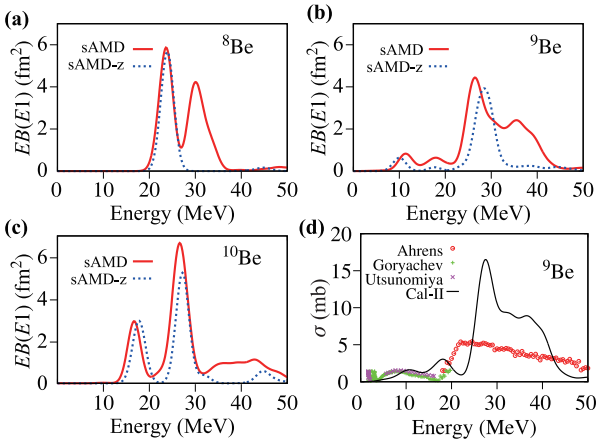

Fig. 15 Energy-weighted $E1$ strengths in (a) ^{8}Be, (b) ^{9}Be, and (c) ^{10}Be obtained by the sAMD calculations. (d) Comparison of the calculated $E1$ strengths with experimental photonuclear cross sections for ^{9}Be [118–120]. The calculated $E1$ strengths are smeared with the width $\gamma = 2$ MeV. Reproduced from Ref. [29].

2α core. In contrast, the shape of the lower peak in ^{9}Be and ^{10}Be is similar to that of ^{8}Be, meaning that the longitudinal oscillation mod is not affected by the excess neutrons.

Let us look at the $E < 20$ MeV region below the IVGDR energy. The IVLED strengths appear in ^{9}Be and ^{10}Be because of the valence neutron motion against the 2α core. In ^{9}Be, the IVLED strengths are well separated from the IVGDR strengths and exhaust about 10% of the energy weighted sum of the calculated $E1$ strengths (20% of the Thomas–Reiche–Kuhn sum rule). This fraction for the LED is consistent with the experimental LED strengths [Fig. 15(d)]. However, the calculation underestimates the width of the IVGDR, maybe, because the model space of the sAMD may not be sufficient to reproduce details of single-particle excitations. In ^{10}Be, the large $E1$ strengths obtained in $E \sim 15$ MeV region correspond to the coherent motion of two neutrons at the surface of the 2α core. The LED modes in ^{10}Be and their isospin characters are discussed in the next section.

6.2.4 Isoscalar monopole and dipole excitations in ^{10}Be

Also in unstable nuclei, IS monopole (ISM) and dipole (ISD) excitations can be good probes for cluster states [30, 69]. In ^{10}Be, the cluster model and AMD calculations predicted the dinuclear cluster resonances of ^{6}He+α in highly excited states above the the MO σ-bond (0^+_2) state (see the upper panel of Fig. 17 and references in the caption). ISM excitations from the ground state in ^{10}Be have been investigated by a ^{6}He+α-cluster model calculation [127]. In the calculation, the ^{6}He+α GCM calculation for the inter-cluster distance R between ^{6}He and α is performed, while taking into account p-shell configurations of the ^{6}He cluster. Details of the calculation are described in Refs. [122, 127]. The calculated ISM strengths are shown in the lower panel of Fig. 17. The ^{6}He+α cluster resonances above the α-decay threshold (10.1 MeV in the calculation) are fragmented into several states because of coupling with discretized continuum states as well as channel coupling. Nevertheless, the

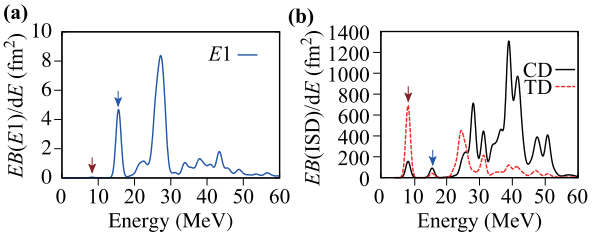

Fig. 16 Energy-weighted dipole strengths, $EB(E1)$, EB(CD), and EB(TD), for $E1$, CD, and TD modes of ^{10}Be calculated with the sAMD+αGCM. The strengths are smeared by the width $\gamma = 1$ MeV. Reproduced from Ref. [121].

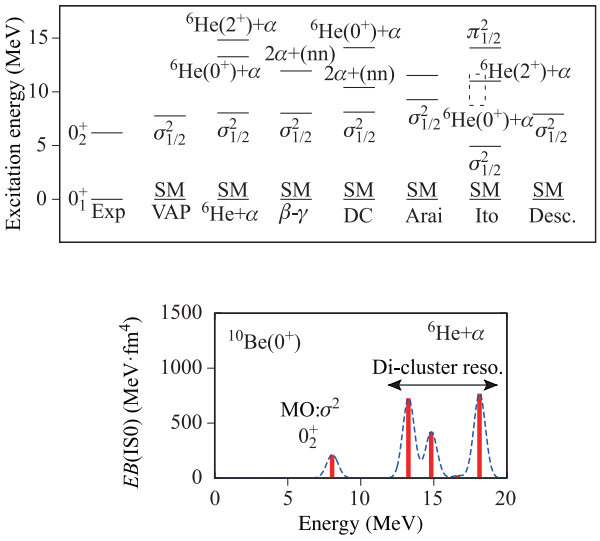

Fig. 17 Top: 0^+ spectra of ^{10}Be. Theoretical energies are those obtained by the AMD+VAP [102], the ^{6}He+α-cluster GCM [122], the $\beta\gamma$-constraint AMD [27], the dineutron condensation(DC)+AMD model [123], the stochastic variational method of $2\alpha + 2n$ by Arai *et al.* [124], the generalized two-center cluster model by Ito *et al.* [125], and the ^{6}He+α-cluster GCM by Descouvemont *et al.* [126]. Bottom: ISM strengths of ^{10}Be obtained by the ^{6}He+α-cluster model calculation [122, 127]. Energy weighted strengths are shown by dashed lines, and those smeared by Gaussian with $\gamma = 1/\sqrt{\pi}$ MeV are shown by solid lines. Reproduced from Refs. [23, 127].

ISM strengths are still concentrated around $E \sim 15$ MeV. The peak in the ISM strengths is dominantly contributed by the ^{6}He(0^+)+α resonance, whereas the broad distribution in $E = 12$–20 MeV contains contributions from both ^{6}He(0^+)+α and ^{6}He(2^+)+α cluster resonances. In contrast to the significant ISM strengths for the cluster resonances in this energy region, the ISM strength of the 0^+_2 state for the MO σ-bond state is small, because the state dominantly contains the ISM transition from the $\pi^2_{3/2}$ configuration in the ground state to the $\sigma^2_{1/2}$ configuration in the 0^+_2 state is hard to occur.

For the dipole excitations, the significant ISLED strengths have been reported in 1980s [128–130]. More detailed strength functions of the ISD excitation have been measured for various stable nuclei in 1990s and 2000s. The separation of the ISLED strengths from the high-energy ISGDR strengths indicates possible appearance of a new type ISD mode different from the compressive dipole (CD) mode for the ISGDR. To understand the origin of the ISLED strengths, a torus mode (or a toroidal dipole (TD) mode) has been proposed by hydro-dynamical models at the early stage [131, 132] and discussed in this decade by microscopic approaches [133–139]. In light nuclei, also cluster states may contribute

to the ISLED strengths because the IS dipole operator excites not only the compressive GRs but also the inter-cluster motion [67]. To clarify natures of dipole excitations in neutron-rich nuclei, the IS and IV characters of the LED strengths have been investigated in experimental and theoretical studies.

We here discuss the $E1$, compressive, and toroidal natures of the dipole excitations in ^{10}Be based on the sAMD+αGCM calculation [121]. Figure 16 shows the calculated CD and TD strengths together with the E1 strengths. In the low-energy region, two kinds of dipole excitations are obtained. One is the the 1^-_1 around 8 MeV and the other is the 1^-_2 around 15 MeV. The latter has the remarkable E1 strength corresponding to the valence neutron oscillation mode against the 2α core as discussed previously. The former has very weak $E1$ strength and is almost invisible in the $E1$ strength function. Instead, the 1^-_1 state has significant IS CD strengths. More interestingly, the 1^-_1 state is remarkably excited by the TD operator indicating that this state has the TD character and is regarded as the TD mode. It means that two different dipole modes exist in the low-energy region, the toroidal dominant 1^-_1 and the $E1$ dominant 1^-_2 states.

To discuss properties of the two LED modes in ^{10}Be, we show the transition current densities for these two 1^- states in Fig. 18. The TD mode is characterized by the vortical nature in the nuclear current, which can be seen in the $0^+_1 \to 1^-_1$ transition current density. The neutron toroidal current gives significant contribution to the TD strength but it gives almost no contribution to the $E1$ strength because it does not contain the translational current. On the other hand, the transition current density for $0^+_1 \to 1^-_2$ shows the translational neutron current at the surface corresponding to the opposite motion of valence neutrons against the 2α core. In this transition, the surface neutron current contributes to the remarkable $E1$ strength, but the internal current from the 2α core motion gives no contribution to the IV strength.

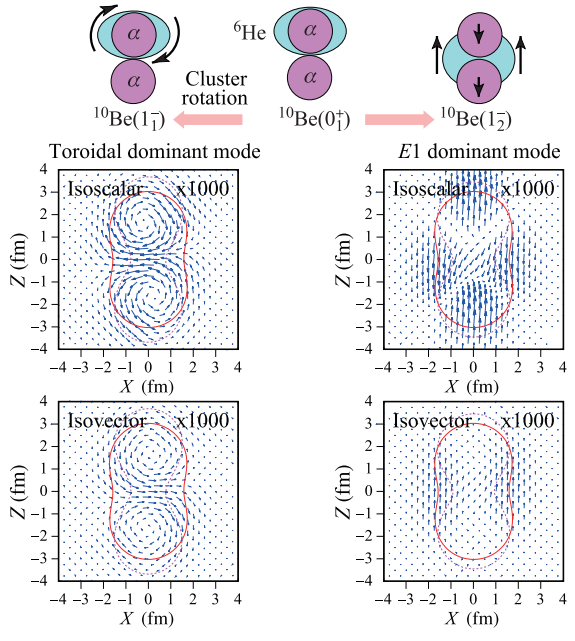

Fig. 18 Vector plots of transition current densities for the toroidal mode ($0^+_1 \to 1^-_1$) and the $E1$ mode ($0^+_1 \to 1^-_2$) in ^{10}Be obtained with the sAMD+αGCM. The isoscalar and isovector contributions of the current densities are plotted on the X–Z plane at $Y = 0$ (scaled by a factor of 10^3). Schematic figures in a cluster picture are also shown. Reproduced from Ref. [121].

It is interesting to give an interpretation for these two LED modes, the toroidal and $E1$ modes, in the cluster picture of $2\alpha+2n$ because the 0^+_1, 1^-_1, and 1^-_2 states have such the cluster structures (see the top panel of Fig. 18). The $0^+_1 \to 1^-_1$ excitation is interpreted as a rotational mode of the deformed ^{6}He cluster. The toroidal neutron flow is caused by the surface neutron current around an α cluster induced by the ^{6}He-cluster rotation. On the other hand, in the $0^+_1 \to 1^-_2$ excitation, the translational neutron current is attributed by the surface neutron oscillation along the longitudinal direction of the 2α core. In the $^6\mathrm{He} + \alpha$ cluster picture, this mode can be interpreted as the $L = 1$ excitation of the relative motion between ^{6}He and α clusters. Moreover, both modes, the ^{6}He-cluster rotation and the valence neutron oscillation, couple with the inter-cluster motion. As a result of the coupling, the significant CD strengths are obtained for the 1^-_1 and 1^-_2 states as already shown in Fig. 16. To test the theoretical prediction, experimental observation of the CD (the normal ISD) strengths by inelastic α scattering on ^{10}Be is requested.

6.3 Linear chain states in neutron-rich C

Possibility of linear-chain nα structure is a long standing problem in theoretical and experimental studies. Appearance of the linear-chain 3α structure in ^{12}C system has been discussed for a long time. In the early stage, the linear-chain 3α structure was proposed to assign $^{12}\mathrm{C}(0^+_2)$ by Morinaga *et al.* [140, 144], but this assignment contradicts the α-decay width [142]. Later, it was found, in 3α-cluster model calculations for ^{12}C, that the $^{12}\mathrm{C}(0^+_2)$ is not the linear-chain 3α state but a weakly bound 3α state like a gas [32–44]. Possibility of the linear-chain 3α structure for higher excited states above the $^{12}\mathrm{C}(0^+_2)$ has been discussed with the cluster models, but such the configuration was found to be unstable against the bending motion [34, 143]. The results of cluster models are supported by the AMD and FMD calculations [22, 25, 45, 46], in which only a bending chain-like structure was predicted in the 0^+_3 state.

Alternatively, the linear-chain 3α structure are ex-

pected in neutron-rich C because it can be stabilized by excess neutrons. In these two decades, intensive studies to search for the linear-chain 3α structure in ^{14}C and ^{16}C have been performed in both the experimental and theoretical sides [109, 110, 143–151].

The $\beta\gamma$-constraint AMD combined with the GCM was applied to ^{14}C and predicted a linear-chain 3α configuration in excited states [109]. The calculated and experimental energy spectra of ^{14}C are shown in Fig. 19. The proton and neutron density distributions of the linear-chain 3α state are also shown in the figure. The linear-chain structure is stabilized by two excess neutrons and constructs a $K^\pi = 0^+$ rotational band just above the ^{10}Be+α threshold energy. The obtained linear-chain states show a $2\alpha + 2n$ correlation and can be interpreted as the ^{10}Be+α structure. As shown in the proton and neutron density distributions, the ^{10}Be cluster is a prolately deformed state containing the 2α core. Another α cluster is located at the head-on position of the deformed ^{10}Be cluster resulting in the aligned 3α configuration in a straight line. In the stabilization mechanism of the linear-chain structure, the excess neutrons contribute to the potential energy gain of the linear-chain structure. In addition, the orthogonal condition to lower states also plays an important role as blocking effect against the bending motion in the linear-chain configuration.

Because of the large prolate deformation, the linear chain structure produces the $K^\pi = 0^+$ band with the small level spacing in the rotational spectra. Recently, candidate states, 0^+, 2^+, and 4^+, for the linear-chain band have been reported by ^{10}Be scattering experiments on α [110, 111]. Also in ^{16}C, a linear chain structure was predicted with a constraint AMD calculation by Baba *et al.* [151].

It should be commented that formation of 3α clusters in ^{14}C is not obvious. Indeed, it is indicated, in the $\beta\gamma$-constraint AMD calculation, that the 3α clustering is weak and even breaking (dissociated) in low-lying states of ^{14,16}C because of the excess neutrons, even though 3α clusters are obtained in the excited states of neutron-rich C.

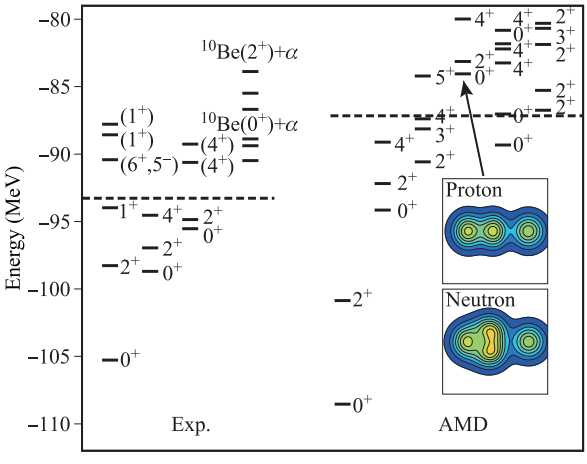

Fig. 19 Energy levels of ^{14}C. The theoretical data are those in Ref. [109] calculated with $\beta\gamma$-constraint AMD+GCM. Proton and neutron density distributions for the linear-chain $K^\pi = 0^+$ band are also shown. The dotted lines are the experimental and theoretical ^{10}Be+α threshold energies. Reproduced from Ref. [109].

7 Summary

We discussed cluster phenomena in light nuclei. As examples of typical cluster structures, cluster structures of light stable nuclei such as ^{12}C, ^{16}O, and ^{20}Ne were explained. Then, some topics of cluster phenomena in light neutron-rich nuclei were introduced. We paid a particular attention on coexistence of cluster and shell-model aspects while focusing on dissolution and formation of α clustering.

As pointed out in the early stage of cluster physics, the cluster formation at the nuclear surface can be understood as the four-nucleons correlation in the major shell and particle-hole excitations. On the other hand, spacial development of clustering is the large amplitude phenomenon of inter-cluster motion beyond the mean-field picture. The continuous description between shell-model and cluster structures became able in microscopic cluster models. In these decades, more flexible models such as the AMD have been developed and enable us to study cluster phenomena in general nuclei including unstable nuclei. These models are also useful to investigate dissolution and formation of α clustering in *sd*-shell and heavier systems, in which the α clustering is more or less dissolved by the spin-orbit mean-potential.

One of the messages is that the cluster aspect is an essential feature of nuclear systems as well as mean-field (shell-model) aspect. This coexistence of two kinds of natures, cluster and shell-model aspects, plays important roles in the ground and excited states, and brings rich phenomena in a wide region of nuclear chart. Moreover, it should be commented that, in the progress of study of cluster phenomena, the concept of nuclear clustering itself has been extended to various phenomena related to many-nucleon correlations beyond the mean-field picture. It is expected that further rich cluster phenomena will be discovered in excited states and heavy-mass nuclei in future experimental and theoretical studies.

Acknowledgements The computational calculations of this work were performed by using the supercomputer in the Yukawa Institute for theoretical physics, Kyoto University. This work was supported by JSPS KAKENHI Grant Nos. 26400270 (Y. K-E.), 16K05351 (H. H.), and 18K03617 (Y. K-E.).

References

1. J. K. Perring and T. H. R. Skyrme, The alpha-particle and shell models of the nucleus, *Proc. Phys. Soc.* 69(8), 600 (1956)
2. B. F. Bayman and A. Bohr, On the connection between the cluster model and the SU_3 coupling scheme for particles in a harmonic oscillator potential, *Nucl. Phys.* 9(4), 596 (1958)
3. A. Arima, H. Horiuchi, and T. Sebe, Weak coupling model of particles and holes in the *sd* shell nuclei, *Phys. Lett. B* 24(3), 129 (1967)
4. F. Nemoto and H. Bando, Alpha-cluster structure and weak coupling feature in light *sd*-shell nuclei, *Prog. Theor. Phys.* 47(4), 1210 (1972)
5. J. A. Wheeler, Molecular viewpoints in nuclear structure, *Phys. Rev.* 52(11), 1083 (1937)
6. J. A. Wheeler, On the mathematical description of light nuclei by the method of resonating group structure, *Phys. Rev.* 52(11), 1107 (1937)
7. K. Wildermuth and T. Kanellopoulos, The "cluster model" of the atomic nuclei, *Nucl. Phys.* 7, 150 (1958)
8. Y. C. Tang, M. LeMere, and D. R. Thompsom, Resonating-group method for nuclear many-body problems, *Phys. Rep.* 47(3), 167 (1978)
9. D. L. Hill and J. A. Wheeler, Nuclear constitution and the interpretation of fission phenomena, *Phys. Rev.* 89(5), 1102 (1953)
10. J. J. Griffin and J. A. Wheeler, Collective motions in nuclei by the method of generator coordinates, *Phys. Rev.* 108(2), 311 (1957)
11. D. M. Brink, in: Proceedings of the International School of Physics Enrico Fermi, Varenna Course 36, 247 (1966)
12. A. Ono, H. Horiuchi, T. Maruyama, and A. Ohnishi, Fragment formation studied with antisymmetrized version of molecular dynamics with two-nucleon collisions, *Phys. Rev. Lett.* 68(19), 2898 (1992)
13. A. Ono, H. Horiuchi, T. Maruyama, and A. Ohnishi, Antisymmetrized version of molecular dynamics with two-nucleon collisions and its application to heavy ion reactions, *Prog. Theor. Phys.* 87(5), 1185 (1992)
14. A. Ono and H. Horiuchi, Antisymmetrized molecular dynamics for heavy ion collisions, *Prog. Part. Nucl. Phys.* 53(2), 501 (2004)
15. Y. Kanada-En'yo, H. Horiuchi, and A. Ono, Structure of Li and Be isotopes studied with antisymmetrized molecular dynamics, *Phys. Rev. C* 52(2), 628 (1995)
16. Y. Kanada-En'yo and H. Horiuchi, Structure of Light Unstable Nuclei Studied with Antisymmetrized Molecular Dynamics, *Prog. Theor. Phys. Suppl.* 142, 205 (2001), arXiv: nucl-th/0107044 [nucl-th]
17. Y. Kanada-En'yo, M. Kimura, and A. Ono, Antisymmetrized molecular dynamics and its applications to cluster phenomena, *Prog. Theor. Exp. Phys.* 2012, 01A202 (2012), arXiv: 1202.1864 [nucl-th]
18. H. Feldmeier, Fermionic molecular dynamics, *Nucl. Phys. A* 515(1), 147 (1990)
19. H. Feldmeier, K. Bieler, and J. Schnack, Fermionic molecular dynamics for ground states and collisions of nuclei, *Nucl. Phys. A* 586(3), 493 (1995)
20. H. Feldmeier and J. Schnack, Molecular dynamics for fermions, *Rev. Mod. Phys.* 72(3), 655 (2000)
21. T. Neff and H. Feldmeier, Tensor correlations in the unitary correlation operator method, *Nucl. Phys. A* 713(3–4), 311 (2003)
22. T. Neff and H. Feldmeier, Cluster structures within fermionic molecular dynamics, *Nucl. Phys. A* 738, 357 (2004)
23. M. Kimura, T. Suhara, and Y. Kanada-En'yo, Antisymmetrized molecular dynamics studies for exotic clustering phenomena in neutron-rich nuclei, *Eur. Phys. J. A* 52, 373 (2016), arXiv: 1612.09432 [nucl-th]
24. Y. Fujiwara, H. Horiuchi, K. Ikeda, M. Kamimura, K. Katō, Y. Suzuki, and E. Uegaki, Comprehensive study of alpha-nuclei, *Prog. Theor. Phys. Suppl.* 68, 29 (1980)
25. Y. Kanada-En'yo, Variation after angular momentum projection for the study of excited states based on antisymmetrized molecular dynamics, *Phys. Rev. Lett.* 81(24), 5291 (1998)
26. M. Kimura, Deformed-basis antisymmetrized molecular dynamics and its application to ^{20}Ne, *Phys. Rev. C* 69(4), 044319 (2004)
27. T. Suhara and Y. Kanada-En'yo, Quadrupole deformation and constraint in a framework of antisymmetrized molecular dynamics, *Prog. Theor. Phys.* 123(2), 303 (2010)
28. Y. Kanada-En'yo, Isoscalar monopole and dipole excitations of cluster states and giant resonances in ^{12}C, *Phys. Rev. C* 93, 054307 (2016), arXiv: 1512.03619 [nucl-th]
29. Y. Kanada-En'yo, Isovector and isoscalar dipole excitations in ^{9}Be and ^{10}Be studied with antisymmetrized molecular dynamics, *Phys. Rev. C* 93, 024322 (2016), arXiv: 1511.08530 [nucl-th]
30. Y. Chiba, M. Kimura, and Y. Taniguchi, Isoscalar dipole transition as a probe for asymmetric clustering, *Phys. Rev. C* 93, 034319 (2016), arXiv: 1512.08214 [nucl-th]
31. M. Freer and H. O. U. Fynbo, The Hoyle state in ^{12}C, *Prog. Part. Nucl. Phys.* 78, 1 (2014)
32. Y. Makita, T. Osaka, and A. Miyazaki, Acoustic phonon softening and spontaneous strains in $KD_3(SeO_3)_2$, *J. Phys. Soc. Jpn.* 44(1), 225 (1978)
33. M. Kamimura, Transition densities between the 01^+, 21^+, 41^+, 02^+, 22^+, 11^- and 31^- states in ^{12}C derived from the three-alpha resonating-group wave functions, *Nucl. Phys. A* 351(3), 456 (1981)

34. E. Uegaki, S. Okabe, Y. Abe, and H. Tanaka, Structure of the excited states in ^{12}C (I), *Prog. Theor. Phys.* 57(4), 1262 (1977)
35. P. Descouvemont and D. Baye, Microscopic theory of the ^{8}Be(α,γ) ^{12}C reaction in a three-cluster model, *Phys. Rev. C* 36(1), 54 (1987)
36. A. Tohsaki, H. Horiuchi, P. Schuck, and G. Röpke, Alpha cluster condensation in ^{12}C and ^{16}O, *Phys. Rev. Lett.* 87, 192501 (2001), arXiv: nucl-th/0110014 [nucl-th]
37. Y. Funaki, A. Tohsaki, H. Horiuchi, P. Schuck, and G. Röpke, Analysis of previous microscopic calculations for the second 0^+ state in ^{12}C in terms of $3-\alpha$ particle Bose-condensed state, *Phys. Rev. C* 67(5), 051306 (2003)
38. S. I. Fedotov, O. I. Kartavtsev, V. I. Kochkin, and A. V. Malykh, 3α-cluster structure of the 0^+ states in ^{12}C and the effective α-α interactions, *Phys. Rev. C* 70(1), 014006 (2004)
39. C. Kurokawa and K. Katō, Three-alpha resonances in ^{12}C, *Nucl. Phys. A* 738, 455 (2004)
40. C. Kurokawa and K. Katō, New broad 0^+ state in ^{12}C, *Phys. Rev. C* 71(2), 021301 (2005)
41. I. Filikhin, V. M. Suslov, and B. Vlahovic, 0^+ states of the ^{12}C nucleus: The Faddeev calculation in configuration space, *J. Phys. G* 31(11), 1207 (2005)
42. K. Arai, Resonance states of ^{12}C in a microscopic cluster model, *Phys. Rev. C* 74(6), 064311 (2006)
43. S. Ohtsubo, Y. Fukushima, M. Kamimura, and E. Hiyama, Complex-scaling calculation of three-body resonances using complex-range Gaussian basis functions: Application to 3α resonances in ^{12}C, *Prog. Theor. Exp. Phys.* 2013, 073D02 (2013)
44. S. Ishikawa, Decay and structure of the Hoyle state, *Phys. Rev. C* 90(6), 061604 (2014)
45. Y. Kanada-En'yo, Structure of ground and excited states of ^{12}C, *Prog. Theor. Phys.* 117, 655 (2007), arXiv: nucl-th/0605047 [nucl-th] [Erratum: *Prog. Theor. Phys.* 121, 895(2009)]
46. M. Chernykh, H. Feldmeier, T. Neff, P. von Neumann-Cosel, and A. Richter, Structure of the Hoyle state in ^{12}C, *Phys. Rev. Lett.* 98(3), 032501 (2007)
47. E. Epelbaum, H. Krebs, T. A. Lähde, D. Lee, and U. G. Meissner, Structure and rotations of the Hoyle state, *Phys. Rev. Lett.* 109(25), 252501 (2012)
48. A. C. Dreyfuss, K. D. Launey, T. Dytrych, J. P. Draayer, and C. Bahri, Hoyle state and rotational features in ^{12}C within a no-core shell-model framework, *Phys. Lett. B* 727(4–5), 511 (2013)
49. J. Carlson, S. Gandolfi, F. Pederiva, S. C. Pieper, R. Schiavilla, K. E. Schmidt, and R. B. Wiringa, Quantum Monte Carlo methods for nuclear physics, *Rev. Mod. Phys.* 87(3), 1067 (2015)
50. N. Takigawa and A. Arima, Structure of ^{12}C, *Nucl. Phys. A.* 168(3), 593 (1971)
51. Y. Funaki, A. Tohsaki, H. Horiuchi, P. Schuck, and G. Röpke, Inelastic form factors to alpha-particle condensate states in ^{12}C and ^{16}O: What can we learn? *Eur. Phys. J. A* 28(3), 259 (2006)
52. F. Ajzenberg-Selove and J. H. Kelley, Energy levels of light nuclei $A = 11$–12, *Nucl. Phys. A.* 506(1), 1 (1990)
53. M. Freer, I. Boztosun, C. A. Bremner, S. P. G. Chappell, R. L. Cowin, et al., Reexamination of the excited states of ^{12}C, *Phys. Rev. C* 76(3), 034320 (2007)
54. M. Itoh, H. Akimune, M. Fujiwara, U. Garg, N. Hashimoto, et al., Candidate for the 2^+ excited Hoyle state at $E_x \sim 10$ MeV in ^{12}C, *Phys. Rev. C* 84(5), 054308 (2011)
55. M. Freer, S. Almaraz-Calderon, A. Aprahamian, N. I. Ashwood, M. Barr, et al., Evidence for a new ^{12}C state at 13.3 MeV, *Phys. Rev. C* 83(3), 034314 (2011)
56. D. J. Marín-Lámbarri, R. Bijker, M. Freer, M. Gai, T. Kokalova, D. J. Parker, and C. Wheldon, Evidence for triangular $\mathcal{D}_{3h}$ symmetry in ^{12}C, *Phys. Rev. Lett.* 113(1), 012502 (2014)
57. M. Freer, H. Horiuchi, Y. Kanada-En'yo, D. Lee, and U.G. Meissner, Microscopic clustering in light nuclei, *Rev. Mod. Phys.* 90, 035004 (2018), arXiv: 1705.06192 [nucl-th]
58. Y. Kanada-En'yo, Y. Shikata, and H. Morita, Cluster and toroidal aspects of isoscalar dipole excitations in ^{12}C, *Phys. Rev. C* 97, 014303 (2018), arXiv: 1709.03045 [nucl-th]
59. T. Suhara, N. Itagaki, J. Cseh, and M. Płoszajczak, Novel and simple description for a smooth transition from α-cluster wave functions to jj-coupling shell model wave functions, *Phys. Rev. C* 87(5), 054334 (2013)
60. T. Suhara and Y. Kanada-En'yo, Effects of a-cluster breaking on 3α-cluster structures in ^{12}C, *Phys. Rev. C* 91(2), 024315 (2015)
61. Y. Funaki, Hoyle band and a condensation in ^{12}C, *Phys. Rev. C* 92(2), 021302 (2015)
62. N. Itagaki, H. Masui, M. Ito, and S. Aoyama, Simplified modeling of cluster-shell competition, *Phys. Rev. C* 71(6), 064307 (2005)
63. B. John, Y. Tokimoto, Y. W. Lui, H. L. Clark, X. Chen, and D. H. Youngblood, Isoscalar electric multipole strength in ^{12}C, *Phys. Rev. C* 68(1), 014305 (2003)
64. M. Chernykh, H. Feldmeier, T. Neff, P. von Neumann-Cosel, and A. Richter, Pair decay width of the Hoyle state and its role for stellar carbon production, *Phys. Rev. Lett.* 105(2), 022501 (2010)
65. T. Kawabata, H. Akimune, H. Fujita, Y. Fujita, M. Fujiwara, et al., $2\alpha+t$ cluster structure in ^{11}B, *Phys. Lett. B* 646(1), 6 (2007)
66. T. Yamada, Y. Funaki, T. Myo, H. Horiuchi, K. Ikeda, G. Röpke, P. Schuck, and A. Tohsaki, Isoscalar monopole excitations in ^{16}O: α-cluster states at low energy and mean-field-type states at higher energy, *Phys. Rev. C* 85(3), 034315 (2012)

67. Y. Chiba and M. Kimura, Cluster states and isoscalar monopole transitions of ^{24}Mg, *Phys. Rev. C* 91, 061302 (2015), arXiv: 1502.06325 [nucl-th]

68. D. H. Youngblood, Y. W. Lui, and H. L. Clark, High lying $E0$ strength in ^{12}C, *Phys. Rev. C* 57(5), 2748 (1998)

69. Y. Kanada-En'yo, Isoscalar monopole and dipole excitations of cluster states and giant resonances in ^{12}C, *Phys. Rev. C* 93, 054307 (2016), arXiv: 1512.03619 [nucl-th]

70. Y. Kanada-En'yo, Cluster states and monopole transitions in ^{16}O, *Phys. Rev. C* 89(2), 024302 (2014)

71. J. P. Elliott and B. H. Flowers, The odd-parity states of ^{16}O and ^{16}N, *Proc. R. Soc. Lond. A* 242(1228), 57 (1957)

72. G. E. Brown and A. M. Green, Even parity states of ^{16}O and ^{17}O, *Nucl. Phys.* 75(2), 401 (1966)

73. Y. Kanada-En'yo, Tetrahedral 4α and ^{12}C+α cluster structures in ^{16}O, *Phys. Rev. C* 96, 034306 (2017), arXiv: 1705.09097 [nucl-th]

74. Y. Funaki, T. Yamada, H. Horiuchi, G. Ropke, P. Schuck, and A. Tohsaki, α-particle condensation in ^{16}O studied with a full four-body orthogonality condition model calculation, *Phys. Rev. Lett.* 101(8), 082502 (2008)

75. Y. Suzuki, Structure study of $T = 0$ states in ^{16}O by ^{12}C+ cluster-coupling model (I), *Prog. Theor. Phys.* 55(6), 1751 (1976)

76. D. R. Tilley, H. R. Weller, and C. M. Cheves, Energy levels of light nuclei $A = 16$–17, *Nucl. Phys. A* 564(1), 1 (1993)

77. T. Wakasa, E. Ihara, K. Fujita, Y. Funaki, K. Hatanaka, et al., New candidate for an alpha cluster condensed state in ^{16}O(α, α') at 400 MeV, *Phys. Lett. B* 653(2–4), 173 (2007)

78. Y. Kanada-En'yo, Cluster states and monopole transitions in ^{16}O, *Phys. Rev. C* 89(2), 024302 (2014)

79. D. M. Brink, H. Friedrich, A. Weiguny, and C. W. Wong, Investigation of the alpha-particle model for light nuclei, *Phys. Lett. B* 33(2), 143 (1970)

80. W. Bauhoff, H. Schultheis, and R. Schultheis, Alpha cluster model and the spectrum of ^{16}O, *Phys. Rev. C* 29(3), 1046 (1984)

81. D. Robson, Evidence for the tetrahedral nature of ^{16}O, *Phys. Rev. Lett.* 42(14), 876 (1979)

82. J. P. Elliott, J. A. Evans, and E. E. Maqueda, α-transfer and a tetrahedral shape for ^{16}O, *Nucl. Phys. A* 437(1), 208 (1985)

83. H. Horiuchi and K. Ikeda, A molecule-like structure in atomic nuclei of ^{16}O* and ^{10}Ne, *Prog. Theor. Phys.* 40(2), 277 (1968)

84. F. D. Becchetti, D. Overway, J. Jänecke, and W. W. Jacobs, ^{12}C(^{6}Li, d)^{16}O at E(Li) = 90 MeV, *Nucl. Phys. A* 344(2), 336 (1980)

85. M. Libert-Heinemann, D. Baye, and P. H. Heenen, Generator-coordinate study of inelastic α+^{12}C scattering, *Nucl. Phys. A* 339(3), 429 (1980)

86. P. Descouvemont, Microscopic description of the 16O spectrum in a multiconfiguration cluster model, *Nucl. Phys. A* 470(2), 309 (1987)

87. P. Descouvemont, Clustering effects in a microscopic four-a description of the α+^{12}C system, *Phys. Rev. C* 44(1), 306 (1991)

88. P. Descouvemont, ^{12}C (α, γ) ^{16}O $E2$ cross section in a microscopic four-alpha model, *Phys. Rev. C* 47(1), 210 (1993)

89. K. Fukatsu and K. Kato, The 4 orthogonality condition model for low-lying 0^+ states of ^{16}O, *Prog. Theor. Phys.* 87(1), 151 (1992)

90. Y. Funaki, T. Yamada, A. Tohsaki, H. Horiuchi, G. Ropke, and P. Schuck, Microscopic study of 4α-particle condensation with inclusion of resonances, *Phys. Rev. C* 82(2), 024312 (2010)

91. W. Horiuchi and Y. Suzuki, Correlated-basis description of a-cluster and delocalized 0^+ states in ^{16}O, *Phys. Rev. C* 89(1), 011304 (2014)

92. Y. Kanada-En'yo and H. Horiuchi, Neutron-rich B isotopes studied with antisymmetrized molecular dynamics, *Phys. Rev. C* 52(2), 647 (1995)

93. Y. Kanada-En'yo and H. Horiuchi, Structure of light unstable nuclei studied with antisymmetrized molecular dynamics, *Prog. Theor. Phys. Suppl.* 142, 205 (2001), arXiv: nucl-th/0107044

94. Y. W. Lui, H. L. Clark, and D. H. Youngblood, Giant resonances in ^{16}O, *Phys. Rev. C* 64(6), 064308 (2001)

95. Y. Akiyama, A. Arima, and T. Sebe, The structure of the *sd* shell nuclei, *Nucl. Phys. A* 138(2), 273 (1969)

96. T. Inoue, T. Sebe, H. Hagiwara, and A. Arima, The structure of the sd-shell nuclei (I): ^{18}C, ^{18}F, ^{19}O, ^{19}F and ^{20}Ne, *Nucl. Phys. A* 59(1), 1 (1964)

97. T. Tomoda and A. Arima, Coexistence of shell structure and cluster structure in ^{20}Ne, *Nucl. Phys. A* 303(1–2), 217 (1978)

98. Y. Kanada-En'yo and H. Horiuchi, Clustering in yrast states of ^{20}Ne studied with antisymmetrized molecular dynamics, *Prog. Theor. Phys.* 93(1), 115 (1995)

99. T. Yamaya, K. Katori, M. Fujiwara, S. Kato, and S. Ohkubo, Alpha-cluster study of ^{40}Ca and ^{44}Ti by the (^{6}Li, d) reaction, *Prog. Theor. Phys. Suppl.* 132, 73 (1998)

100. M. Kimura and H. Horiuchi, Coexistence of cluster structure and superdeformation in ^{44}Ti, *Nucl. Phys. A* 767, 58 (2006)

101. Y. Kanada-En'yo, in: Proceedings of the International School of Physics Enrico Fermi, Varenna Course 201, 2018

102. Y. Kanada-En'yo, H. Horiuchi, and A. Doté, Structure of excited states of ^{10}Be studied with antisymmetrized molecular dynamics, *Phys. Rev. C* 60(6), 064304 (1999)

103. W. Nörtershäuser, D. Tiedemann, M. Žáková, Z. Andjelkovic, K. Blaum, et al., Nuclear charge radii of ^{7,9,10}Be and the one-neutron halo nucleus ^{11}Be, *Phys. Rev. Lett.* 102(6), 062503 (2009)

104. A. Krieger, K. Blaum, M. L. Bissell, N. Frömmgen, C. Geppert, M. Hammen, K. Kreim, M. Kowalska, J. Krämer, T. Neff, R. Neugart, G. Neyens, W. Nörtershäuser, C. Novotny, R. Sánchez, and D. T. Yordanov, Nuclear charge radius of ^{12}Be, *Phys. Rev. Lett.* 108(14), 142501 (2012)

105. Y. Kanada-En'yo, Proton radii of Be, B, and C isotopes, *Phys. Rev. C* 91(1), 014315 (2015)

106. W. von Oertzen, M. Freer, and Y. Kanada-En'yo, Nuclear clusters and nuclear molecules, *Phys. Rep.* 432(2), 43 (2006)

107. W. von Oertzen, Covalently bound molecular structures in the α+^{16}O system, *Eur. Phys. J. A* 11(4), 403 (2001)

108. M. Kimura, Molecular orbitals and $\alpha + $ O 18 molecular bands of ^{22}Ne, *Phys. Rev. C* 75(3), 034312 (2007)

109. T. Suhara and Y. Kanada-En'yo, Cluster structures of excited states in ^{14}C, *Phys. Rev. C* 82(4), 044301 (2010)

110. A. Fritsch, S. Beceiro-Novo, D. Suzuki, W. Mittig, J. J. Kolata, et al., One-dimensionality in atomic nuclei: A candidate for linear-chain a clustering in ^{14}C, *Phys. Rev. C* 93(1), 014321 (2016)

111. H. Yamaguchi, D. Kahl, S. Hayakawa, Y. Sakaguchi, K. Abe, et al., Experimental investigation of a linear-chain structure in the nucleus ^{14}C, *Phys. Lett. B* 766, 11 (2017)

112. M. Milin, M. Zadro, S. Cherubini, T. Davinson, A. Di Pietro, et al., Sequential decay reactions induced by a 18 MeV ^{6}He beam on ^{6}Li and ^{7}Li, *Nucl. Phys. A* 753(3–4), 263 (2005)

113. M. Freer, E. Casarejos, L. Achouri, C. Angulo, N. I. Ashwood, et al., α:2n:α molecular band in ^{10}Be, *Phys. Rev. Lett.* 96(4), 042501 (2006)

114. S. Okabe, Y. Abe, and H. Tanaka, The structure of ^{9}Be nucleus by a molecular model (I), *Prog. Theor. Phys.* 57(3), 866 (1977)

115. W. von Oertzen, Two-center molecular states in ^{9}B, ^{9}Be, ^{10}Be, and ^{10}B, *Z. Phys. A* 354(1), 37 (1996)

116. M. Seya, N. Kohno, and S. Nagata, Nuclear binding mechanism and structure of neutron-rich Be and B isotopes by molecular-orbital model, *Prog. Theor. Phys.* 65(1), 204 (1981)

117. N. Itagaki and S. Okabe, Molecular orbital structures in ^{10}Be, *Phys. Rev. C* 61(4), 044306 (2000)

118. J. Ahrens, H. Borchert, K. H. Czock, H. B. Eppler, H. Gimm, H. Gundrum, M. Kröning, P. Riehn, G. Sita Ram, A. Zieger, and B. Ziegler, Total nuclear photon absorption cross sections for some light elements, *Nucl. Phys. A* 251(3), 479 (1975)

119. A. Goryachev, G. Zalesnyy, I. Pozdnev, and I. Rossiiskoi, *Akad. Nauk Ser. Fiz.* 56, 159 (1992)

120. H. Utsunomiya, S. Katayama, I. Gheorghe, S. Imai, H. Yamaguchi, D. Kahl, Y. Sakaguchi, T. Shima, K. Takahisa, and S. Miyamoto, Photodisintegration of ^{9}Be through the $1/2^+$ state and cluster dipole resonance, *Phys. Rev. C* 92(6), 064323 (2015)

121. Y. Kanada-En'yo and Y. Shikata, Toroidal, compressive, and $E1$ properties of low-energy dipole modes in ^{10}Be, *Phys. Rev. C* 95, 064319 (2017), arXiv: 1704.05649 [nucl-th]

122. Y. Kanada-En'yo and T. Suhara, ^{6}He-triton cluster states in ^{9}Li, *Phys. Rev. C* 85(2), 024303 (2012)

123. F. Kobayashi and Y. Kanada-En'yo, Novel cluster states in ^{10}Be, *Phys. Rev. C* 86(6), 064303 (2012)

124. K. Arai, Structure of the excited states of ^{10}Be in a microscopic cluster model, *Phys. Rev. C* 69(1), 014309 (2004)

125. M. Ito and K. Ikeda, Unified studies of chemical bonding structures and resonant scattering in light neutron-excess systems ^{10,12}Be, *Rep. Prog. Phys.* 77(9), 096301 (2014)

126. P. Descouvemont, Microscopic study of a clustering in the ^{9,10,11}Be isotopes, *Nucl. Phys. A* 699(3–4), 463 (2002)

127. Y. Kanada-En'yo, Monopole transitions to cluster states in ^{10}Be and ^{9}Li, *Phys. Rev. C* 94, 024326 (2016), arXiv: 1604.01453 [nucl-th]

128. M. N. Harakeh and A. E. L. Dieperink, Isoscalar dipole resonance: Form factor and energy weighted sum rule, *Phys. Rev. C* 23(5), 2329 (1981)

129. P. Decowski, H. P. Morsch, and W. Benenson, Low-lying isoscalar dipole excitations in ^{208}Pb, *Phys. Lett. B* 101(3), 147 (1981)

130. T. D. Poelhekken, S. K. B. Hesmondhalgh, H. J. Hofmann, A. van der Woude, and M. N. Harakeh, Low-energy isoscalar dipole strength in ^{40}Ca, ^{58}Ni, ^{90}Zr and ^{208}Pb, *Phys. Lett. B* 278(4), 423 (1992)

131. S. F. Semenko, Vortex waves in nuclei, *Sov. J. Nucl. Phys.* 34, 356 (1981)

132. D. G. Ravenhall and J. Wambach, Nuclear transition currents and vorticity, *Nucl. Phys. A* 475(3), 468 (1987)

133. N. Paar, D. Vretenar, E. Khan, and G. Colo, Exotic modes of excitation in atomic nuclei far from stability, *Rept. Prog. Phys.* 70, 691 (2007), arXiv: nucl-th/0701081

134. D. Vretenar, N. Paar, P. Ring, and T. Nikšić, Toroidal dipole resonances in the relativistic random phase approximation, *Phys. Rev. C* 65(2), 021301 (2002)

135. N. Ryezayeva, T. Hartmann, Y. Kalmykov, H. Lenske, P. von Neumann-Cosel, V. Yu. Ponomarev, A. Richter, A. Shevchenko, S. Volz, and J. Wambach, Nature of low-energy dipole strength in nuclei: The case of a resonance at particle threshold in ^{208}Pb, *Phys. Rev. Lett.* 89(27), 272502 (2002)

136. P. Papakonstantinou, V. Yu. Ponomarev, R. Roth, and J. Wambach, Isoscalar dipole coherence at low energies and forbidden E1 strength, *Eur. Phys. J. A* 47(1), 14 (2011)

137. J. Kvasil, V. O. Nesterenko, W. Kleinig, P. G. Reinhard, and P. Vesely, General treatment of vortical, toroidal, and compression modes, *Phys. Rev. C* 84(3), 034303 (2011)

138. A. Repko, P. G. Reinhard, V. O. Nesterenko, and J. Kvasil, Toroidal nature of the low-energy E1 mode, *Phys. Rev. C* 87(2), 024305 (2013)

139. V. O. Nesterenko, J. Kvasil, A. Repko, W. Kleinig, and P. G. Reinhard, Toroidal resonance: relation to pygmy mode, vortical properties and anomalous deformation splitting, *Phys. Atom. Nucl.* 79(6), 842 (2016), arXiv: 1602.03326 [nucl-th]

140. H. Morinaga, Interpretation of some of the excited states of 4 n self-conjugate nuclei, *Phys. Rev.* 101(1), 254 (1956)

141. H. Morinaga, On the spin of a broad state around 10 MeV in ^{12}C, *Phys. Lett.* 21(1), 78 (1966)

142. Y. Suzuki, H. Horiuchi, and I. Ikeda, Study of a chain states through their decay widths, *Prog. Theor. Phys.* 47(5), 1517 (1972)

143. N. Itagaki, S. Okabe, K. Ikeda, and I. Tanihata, Molecular-orbital structure in neutron-rich C isotopes, *Phys. Rev. C* 64, 014301 (2001), arXiv: nuclth/0103047

144. W. von Oertzen, M. Freer, and Y. Kanada-En'yo, Nuclear clusters and nuclear molecules, *Phys. Rep.* 432(2), 43 (2006)

145. N. Soić, M. Freer, L. Donadille, N. M. Clarke, P. J. Leask, W. N. Catford, K. L. Jones, D. Mahboub, B. R. Fulton, B. J. Greenhalgh, D. L. Watson, and D. C. Weisser, ^{4}He decay of excited states in ^{14}C, *Phys. Rev. C* 68(1), 014321 (2003)

146. W. von Oertzen, H. G. Bohlen, M. Milin, T. Kokalova, S. Thummerer, A. Tumino, R. Kalpakchieva, T. N. Massey, Y. Eisermann, G. Graw, T. Faestermann, R. Hertenberger, and H. F. Wirth, Search for cluster structure of excited states in ^{14}C, *Eur. Phys. J. A* 21(2), 193 (2004)

147. D. L. Price, M. Freer, N. I. Ashwood, N. M. Clarke, N. Curtis, L. Giot, V. Lima, P. M. Ewan, B. Novatski, N. A. Orr, S. Sakuta, J. A. Scarpaci, D. Stepanov, and V. Ziman, a decay of excited states in ^{14}C, *Phys. Rev. C* 75(1), 014305 (2007)

148. P. J. Haigh, N. I. Ashwood, T. Bloxham, N. Curtis, M. Freer, P. McEwan, D. Price, V. Ziman, H. G. Bohlen, T. Kokalova, C. Schulz, R. Torabi, W. Oertzen, C. Wheldon, W. Catford, C. Harlin, R. Kalpakchieva, and T. N. Massey, Measurement of a and neutron decay widths of excited states of ^{14}C, *Phys. Rev. C* 78(1), 014319 (2008)

149. J. A. Maruhn, N. Loebl, N. Itagaki, and M. Kimura, Linear-chain structure of three α-clusters in ^{16}C and ^{20}C, *Nucl. Phys. A* 833(1–4), 1 (2010)

150. M. Freer, J. D. Malcolm, N. L. Achouri, N. I. Ashwood, D. W. Bardayan, S. M. Brown, W. N. Catford, K. A. Chipps, J. Cizewski, N. Curtis, K. L. Jones, T. Munoz-Britton, S. D. Pain, N. Soić, C. Wheldon, G. L. Wilson, and V. A. Ziman, Resonances in ^{14}C observed in the ^{4}He(^{10}Be, α) ^{10}Be reaction, *Phys. Rev. C* 90(5), 054324 (2014)

151. T. Baba, Y. Chiba, and M. Kimura, 3α clustering in excited states of ^{16}C, *Phys. Rev. C* 90(6), 064319 (2014)